



Effect of blockage on wind turbine power and wake development

Olivier Ndindayino, Augustin Puel, and Johan Meyers

Department of Mechanical Engineering, KU Leuven, Celestijnenlaan 300, B3001 Leuven, Belgium

Correspondence: Olivier Ndindayino (olivier.ndindayino@kuleuven.be)

Received: 14 January 2025 – Discussion started: 12 February 2025

Revised: 2 June 2025 – Accepted: 11 July 2025 – Published: 25 September 2025

Abstract. Recent work by Lanzilao and Meyers (2024) has shown that wind-farm blockage introduces an unfavourable pressure gradient in front of the farm and a favourable pressure gradient in the farm, which are strongly correlated with the nonlocal efficiency and wake efficiency, respectively. In particular, the favourable pressure gradient in the farm increases the farm wake efficiency, defined as the average farm power normalized by the average front-row power. Here, we investigate the impact of blockage on wake development and the power of wind turbines using an idealized large-eddy simulation setup in which blockage conditions are artificially introduced using a rigid lid, in addition to using neutral stratification and no wind veer. We simulate both infinite and finite single turbine rows, as well as a setup with two staggered rows. Blockage strength is adjusted by varying the boundary layer height (H) and turbine spacing (S). We find that blockage strongly affects near-wake behaviour, altering Froude momentum theory, by introducing a favourable pressure difference (Δp_{NW}) across the turbine row. The same setup also leads to an unfavourable pressure difference (Δp_{FW}) in the far wake, which simply follows from the rigid-lid conditions and the change in momentum flux due to wake recovery. A strong positive correlation of $-\Delta p_{NW}$ with both the power coefficient (C_P) and thrust coefficient (C_T) is observed. Specifically, as S and H decrease, $-\Delta p_{NW}$, C_P , and C_T increase. At the same time, a lower induction is observed at the rotor disc, and a lower wake deficit, in the near wake. The reduction of near-wake velocity deficit as a result of blockage also translates into lower deficits and wake widths in the far wake. When scaling the far-wake development with the initial far-wake deficit and width, we do not see a direct effect of the adverse pressure gradient on the wake recovery. However, we do see a profound effect of H on the wake spreading, with higher boundary layers leading to faster spreading. This relates to the fact that the wake can more freely expand vertically in high-boundary layer cases into a larger region of high-speed flow than for shallow boundary layers. Finally, we introduce a simplified Froude momentum balance to parameterize the relation between blockage, pressure drop, and near-wake properties and compare it to the large-eddy simulation results.

1 Introduction

In large wind farms, significant flow slowdown occurs upstream of the farm, called blockage. Measurements conducted by Bleeg et al. (2018) before and after wind-farm commissioning revealed significant reductions of wind speed upstream of the farm (up to 4 % for 10 rotor diameters). Around the same time, Allaerts and Meyers (2017, 2018) described the excitation of gravity waves in their wind-farm large-eddy simulations (LESs), also observing significant slow down of wind speed in front of the farm. Since then,

various other studies have also discussed the excitation of gravity waves by wind farms and related blockage effects (Wu and Porté-Agel, 2017; Maas, 2023; Stipa et al., 2024). Recently, Lanzilao and Meyers (2024) performed LESs of a fixed 1.6 GW wind farm in different atmospheric stratified conditions to investigate effects on wind-farm efficiency, blockage, and related gravity-wave excitation. They found that the upstream slowdown associated with blockage mainly originates from the vertical displacement of the capping inversion at the top the boundary layer and the associated hy-

drostatic pressure induced by the increased column of cold (higher density) air below the inversion. For the atmosphere conditions considered in their simulations, purely hydrodynamic blockage effects (i.e. associated with Bernoulli's law and induction by the turbines; see also Segalini and Dahlberg, 2020) were at least an order of magnitude smaller (Lanzilao and Meyers, 2022, 2024).

Similar to Allaerts and Meyers (2017, 2018), Lanzilao and Meyers (2024) identified a strong unfavourable pressure gradient upstream of the farm, but they also identified a favourable pressure gradient within the wind farm. They defined the nonlocal efficiency $\eta_{nl} = P_1/P_\infty$ as the ratio between the power of a freestanding turbine P_∞ and the average turbine power of the first row of a wind farm P_1 , and they defined the wake efficiency $\eta_w = P_{tot}/(N_t P_1)$ as the ratio between the average turbine power in the wind farm (P_{tot}/N_t) and the average turbine power of the first row. A strong negative correlation was found between the unfavourable upstream pressure gradient and η_{nl} and a strong positive correlation between the favourable pressure gradient within the farm and η_w . Additionally, for wind farms in the conventionally neutral boundary layer, depending on the atmospheric conditions, the beneficial effects of the favourable pressure gradient can offset the negative effects of the upstream unfavourable pressure gradient, sometimes leading to a larger farm efficiency than in a similar fully neutral case without free-atmosphere stratification.

In the current paper, our aim is to better understand the relationship between a favourable pressure gradient and improved efficiency using a new set of large-eddy simulations. To this end, we strongly simplify the simulation setup by replacing blockage induced by free-atmosphere stratification with blockage induced by a rigid lid at the top of the boundary layer. Such a rigid-lid condition could be the equivalent of an infinitely strong capping inversion. Although such a condition cannot exist, because the strongest density jump conceivable over the capping inversion should be well below the difference between density at 1 atm and vacuum, rigid-lid blockage nonetheless shows some similarities with blockage induced by free-atmosphere stratification (Smith, 2024). The advantage of using a rigid-lid condition is that the relationship between blockage, pressure gradient, and efficiency is easier to quantify. This is illustrated in Fig. 1 for a single, infinitely wide row of turbines. Looking at a control volume around the near wake and induction region of a turbine, it is directly clear that a favourable pressure difference should exist ($\Delta p_{NW} < 0$) – presuming negligible friction at the ground, this is a direct result of Newton's second law, the presence of the turbine thrust force, and continuity (such that outflowing momentum is larger than inflowing momentum). Similarly, an unfavourable pressure difference ($\Delta p_{FW} > 0$) should apply in the far wake. Moreover, applying the conservation of momentum in the streamwise direction, considering the entire domain shown in Fig. 1 for an infinite row, that is, from the beginning of the induction zone to the end of the

far wake, as wide as the turbine spacing S and as high as the boundary layer height H , we find:

$$HS(\Delta p_{NW} + \Delta p_{FW} + \Delta p_{bg}) + F_T + F_{fric} = 0, \quad (1)$$

where $F_T (> 0)$ is the turbine thrust, $F_{fric} (> 0)$ is the friction from the ground, and $\Delta p_{bg} (< 0)$ is the background pressure difference in the absence of the turbines. We remark that the velocity profile at the end of the far wake has recovered back to the velocity profile at the start of the induction zone; therefore, no change in momentum is present in Eq. (1). We assume that $F_{fric} \approx \Delta p_{bg}$; thus, Δp_{NW} and Δp_{FW} are dynamic pressure perturbations, superimposed on the background pressure. This simplifies Eq. (1) to $-\Delta p_{NW} \approx \Delta p_{FW} + F_T/HS$, and thus $-\Delta p_{NW} > \Delta p_{FW}$, from which we hypothesize that the effect of blockage on efficiency is mostly related to changes in the near-wake behaviour.

The effects of domain blockage by rigid boundaries on turbine performance have been studied before, mostly in the context of blockage corrections in wind tunnel experiments of single model wind turbines (Mikkelsen and Sørensen, 2002; Werle, 2010; Segalini and Inghels, 2014). In these studies, the focus was on estimating free-flow conditions, thus eliminating the effects of wind tunnel walls. These corrections were built by extending Froude momentum theory (Froude, 1889) to account for the pressure gradients included by any (small) domain blockage present in the wind tunnel. Here, we will use similar ideas to develop a simple model that correlates favourable pressure gradients induced by blockage with near-wake induction and turbine power extraction, but now to quantify the effect of blockage rather than to exclude it. A similar approach was already used by Garrett and Cummins (2007) for tidal turbines in constant water level channels, and some elements were also used by Nishino and Willden (2012, 2013) for modelling the blockage effect of a finite array of tidal turbines in a wide channel cross-section.

The setup of a row of closely spaced turbines that we are studying in the current work has also been explored in the past by McTavish et al. (2013, 2015) and Strickland and Stevens (2020, 2022). They reported so called “in-field” blockage, leading to increased power production of the turbines, which they attributed to mutual favourable interactions between turbines. However, by performing a careful domain sensitivity study, Bleeg and Montavon (2022) later showed that these beneficial effects disappear when the domain size is sufficiently large. Thus, in these earlier reports, power increase due to “in-field” blockage was effectively a result of domain blockage and consequently may be related to the increased wake efficiency observed by Lanzilao and Meyers (2024) under favourable pressure gradient conditions.

Looking at the sketch in Fig. 1 and referring to the discussion above, an unfavourable pressure gradient is expected in the far wake, albeit smaller than the favourable pressure gradient in the near wake. The effects of pressure gradients on

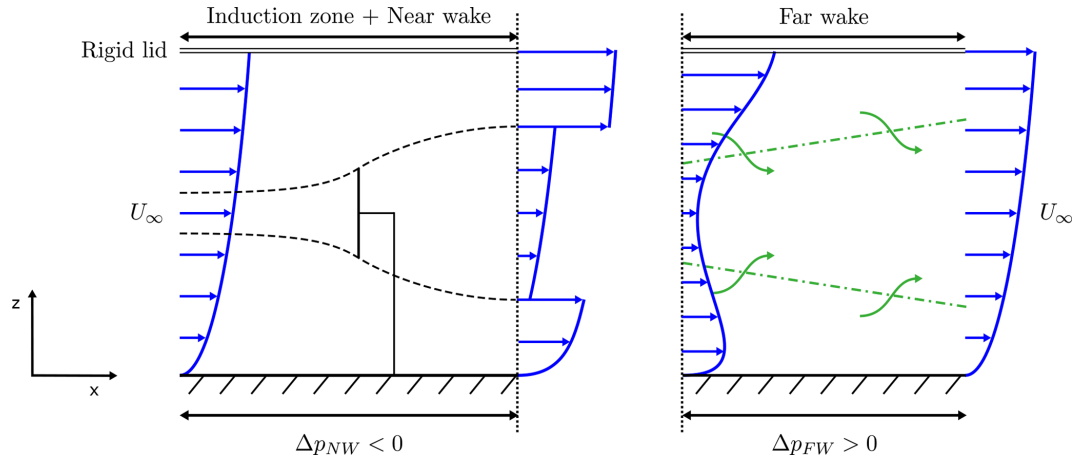


Figure 1. Sketch (side view) of a single turbine row (infinitely wide) inside an idealized atmospheric boundary layer with the rigid-lid top condition.

wake development have been studied by Liu et al. (2002) and Shamsoddin and Porté-Agel (2017) for plane wakes and by Shamsoddin and Porté-Agel (2018) for axisymmetric wakes, and later more general conditions were considered by Dar and Porté-Agel (2022). All of these studies conclude that unfavourable pressure gradients lead to slower wake recovery and favourable pressure gradients lead to faster wake recovery. However, we note already that for all simulations considered in the current paper, we found the unfavourable pressure gradients in the far wake to be much smaller than the values appearing in the above studies such that wake recovery is unaffected by them.

In the current work, we set up a range of large-eddy simulations of a neutral rigid-lid pressure-driven boundary layer, in which we represent both infinite and finite single turbine rows, as well as a setup with staggered rows. Blockage strength is adjusted by varying the boundary layer height (H) and turbine spacing (S). Simulation results are further compared to a simple model that extends classical Froude momentum theory, parameterizing the effects of pressure gradients on wind turbine power, thrust, and induction. Such a model can straightforwardly be incorporated into engineering blockage and wake models such as WAYVE (Allaerts and Meyers, 2019; Devesse et al., 2022; Stipa et al., 2024; Devesse et al., 2024a, b), in which large-scale pressure gradients coming from free-atmosphere stratification and gravity wave feedback are available. The latter is, however, a topic of future research and not in the scope of the current paper.

The article is structured as follows. The setup of the LESs is elaborated in Sect. 2. The extension of Froude momentum theory is discussed in Sect. 3. Next, Sect. 4 presents the LES results for the far- and near-wake analysis, including model validation. Lastly, conclusions are provided in Sect. 5.

2 Methodology

2.1 Governing equations

We consider the filtered Navier–Stokes equations for a neutral pressure-driven boundary layer, given by

$$\frac{\partial \tilde{u}_i}{\partial x_i} = 0, \quad (2)$$

$$\frac{\partial \tilde{u}_i}{\partial t} + \tilde{u}_j \frac{\partial \tilde{u}_i}{\partial x_j} = -\frac{1}{\rho} \frac{\partial \tilde{p}^*}{\partial x_i} - \frac{1}{\rho} \frac{dp_\infty}{dx_1} \delta_{1i} - \frac{\partial \tau_{ij}^{\text{sgs}}}{\partial x_j} + f_i, \quad (3)$$

where the horizontal and vertical directions are represented by indices $i = 1, 2$, and 3 , with $(x_1, x_2, x_3) = (x, y, z)$. The filtered velocity components are denoted by \tilde{u}_i for the three-dimensional flow field, with $(\tilde{u}_1, \tilde{u}_2, \tilde{u}_3) = (\tilde{u}, \tilde{v}, \tilde{w})$. The filtered modified pressure is defined as $\tilde{p}^* = \tilde{p} - p_\infty + \rho_0 \tau_{kk}/3$, where p_∞ represents the mean background pressure and $\tau_{kk}/3$ denotes the trace of the subgrid-scale stress tensor $\tau_{ij} = \tilde{u}_i \tilde{u}_j - \tilde{u}_i \tilde{u}_j$, and where a subgrid-scale model is used to model the anisotropic component of the residual-stress tensor $\tau_{ij}^{\text{sgs}} = \tau_{ij} - \delta_{ij} \tau_{kk}/3$. Note that the direct effect of viscosity on resolved scales in the LES is negligible; all the dissipation is handled by the subgrid-scale stresses. The forces (per unit of density) f_i exerted by the wind turbines on the flow are modelled using a non-rotating actuator disc model (Goit and Meyers, 2015) with a Shapiro correction factor (Shapiro et al., 2019) to avoid over prediction of turbine power on typical LES grid resolutions.

The governing Eqs. (2)–(3) are solved using the SP-Wind solver, an in-house software developed at KU Leuven (Calaf et al., 2010; Goit and Meyers, 2015; Munters et al., 2016b; Allaerts and Meyers, 2017; Lanzilao and Meyers, 2024). The equations are integrated over time using a standard fourth-order Runge–Kutta scheme, with the time step determined by a Courant–Friedrichs–Lewy (CFL) number of 0.4. Discretization in the horizontal direction is performed using a

Fourier pseudo-spectral method, employing the 3/2 dealiasing rule. In the vertical direction, an energy-preserving fourth-order finite difference scheme is applied (Verstappen and Veldman, 2003). Continuity is enforced by direct solving the Poisson equation at each stage of the Runge–Kutta method. The influence of subgrid-scale motions on the resolved flow is captured by the Smagorinsky model in combination with Mason and Thomson (1992) wall damping, using a Smagorinsky length $\ell_s^{-n} = (C_s \Delta)^{-n} + [\kappa(z + z_0)]^{-n}$, with $C_s = 0.14$, $n = 1$, $\Delta = (\Delta x \Delta y \Delta z)^{1/3}$ the grid spacing, and $\kappa = 0.41$ the Von Kármán constant. This is consistent with prior studies using SP-Wind (Meyers, 2011; Allaerts and Meyers, 2017; Lanzilao and Meyers, 2024). We also refer to Calaf et al. (2010), Lignarolo et al. (2016), Martínez-Tossas et al. (2018), and Sood et al. (2022) for code benchmarking and validation.

2.2 Simulation setup

Figure 2 provides an overview of the different simulations setups considered in the current study, and a list of all cases is provided in Table 1. All turbines correspond to the International Energy Agency (IEA) 15 MW offshore reference wind turbine (Gaertner et al., 2020), with hub height $z_h = 150$ m and diameter $D = 240$ m. Conditions are such that the turbines operate below their rated power. Consequently, a constant disc-based thrust coefficient, $C_t' = 1.44$ (Calaf et al., 2010), is used as an input parameter for the simulations.

First of all, a set of single infinite row simulations is considered (Fig. 2a). We select a domain width $L_y = 9.6$ km with spanwise periodic boundary conditions, and by varying the number of turbines in the domain, we can change the turbine spacing S . Secondly, we also consider a finite row setup consisting of seven turbines (Fig. 2b). Here, we take $L_y = 50$ km, so that $L_y/L_y^f \approx 7$ for the case with widest spacing ($S = 5$), following Lanzilao and Meyers (2024), who recommend $L_y/L_y^f \geq 6$ to avoid artificial effects from spanwise boundaries. Finally (Fig. 2c), two infinitely wide staggered rows of turbines are considered, with $S_x/D = 5$, also using a domain width of $L_y = 9.6$ km.

The simulation domain $L_x \times L_y \times H$ is further selected as follows. All simulations use $L_x = 20$ km, with an upstream region $L_{\text{ind}} = 4$ km in front of the turbines and a fringe region length $L_{\text{fr}} = 2.6$ km. Different boundary layer heights are considered, i.e. $H = 350, 500$, and 700 m. All simulations use wall stress boundary conditions at the bottom (with a surface roughness $z_0 = 10^{-4}$ m, which is a typical offshore value (Taylor and Yelland, 2001)) and symmetry conditions at the top. Boundary conditions in the horizontal direction are periodic, as a result of our pseudo-spectral discretization method. To break the periodicity in the streamwise direction and prescribe an inflow condition, we use a fringe-region technique to drive the main domain by turbulent, fully developed, statistically steady flow fields obtained from a concurrent precursor simulation (Stevens et al., 2014). Using a pre-

cursor simulation ensures that turbulent inflow conditions are generated directly by the Navier–Stokes equations, thereby enhancing the accuracy and realism of the inflow turbulence (Munters et al., 2016a).

To prevent persistent spanwise locking of large-scale streamwise turbulent structures, a shifted periodic boundary condition is applied within the fringe region, bypassing the need for excessive streamwise domain lengths (Munters et al., 2016b).

The precursor simulation domain $L_x^p \times L_y^p \times H$ is defined as follows. Three different precursor simulations are performed for the infinite row cases, i.e. $L_x^p = 10$ km and $L_y^p = 9.6$ with a height of $H = 350, 500$, and 700 m. One additional precursor simulation is performed for the finite row cases, with $L_x^p = L_y^p = 10$ km and $H = 500$ m. However, because the fringe region spans the full width and height of the main domain, SP-Wind requires matching heights and widths between the precursor and main domain when they run concurrently. To achieve this, the tiling technique of Sanchez Gomez et al. (2023) is used to extend the precursor flow fields in the y direction from 10 to 50 km.

All precursor simulations are driven by a constant pressure gradient $dp_\infty/dx_1 = -u_\tau^2/H$, with a friction velocity $u_\tau \approx 0.275 \text{ m s}^{-1}$, typical for offshore conditions (Lanzilao and Meyers, 2024). Fixing u_τ yields approximately the same hub-height wind speed for a given z_0 and varying H simulations. Finally, all simulations and domains use the same grid resolution, i.e. $\Delta x = 40$ m, $\Delta y = 24$ m, and $\Delta z = 7.93$ m in the streamwise, spanwise, and vertical directions, respectively. This is consistent with resolutions used earlier in, e.g., Allaerts and Meyers (2017, 2018); Lanzilao and Meyers (2024).

Precursor simulations are initialized using a log profile $u = (u_\tau/\kappa) \ln(z/z_0)$ in combination with random noise and simulated for 20 000 s, such that a fully developed, statistically stationary, pressure-driven boundary layer can develop. Subsequently, the precursor domain and main domain are run concurrently for another 3000 s for the main domain to fully develop given the precursor inflow. Finally, the precursor and main domain are concurrently progressed for an average time T_{av} of 10 000 s.

3 Froude momentum theory with blockage

We extend the Froude momentum theory to parameterize the relation between blockage, pressure drop, and near-wake properties for a single turbine present within a row or farm. The model is an extension of classic axial momentum theory developed by Rankine (1865) and Froude (1889). A similar approach was, e.g., used by Werle (2010) and Segalini and Inghels (2014) to derive blockage corrections for wind tunnels or by Garrett and Cummins (2007) in the context of tidal turbines, although we start from a slightly more general for-

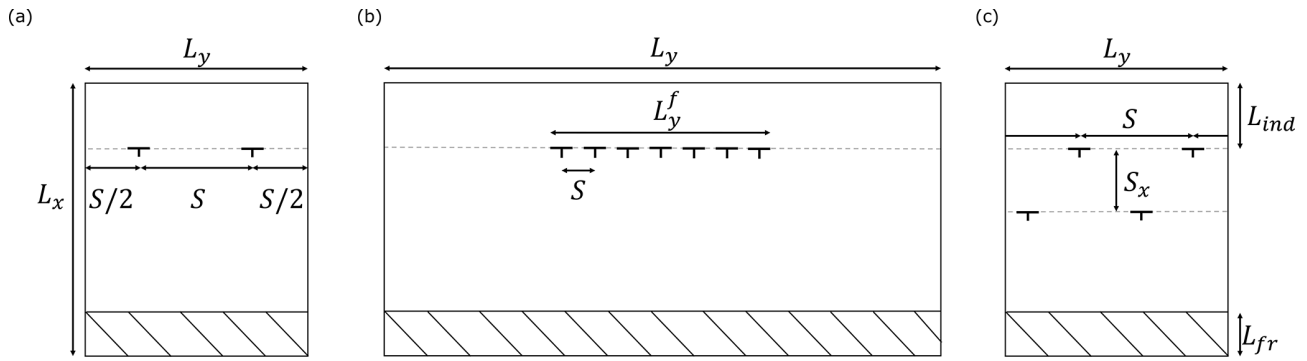


Figure 2. The plan view of the (a) infinite row, (b) finite row, and (c) infinite staggered rows main computational domains.

Table 1. Overview of the wind-farm simulation cases and their computational domain dimensions $L_x \times L_y \times H$, the turbine spacing S/D , the row averaged power coefficient $\langle C_P \rangle_{\text{row}}$, and the thrust coefficient $\langle C_T \rangle_{\text{row}}$ (values of both rows are shown for the infinite staggered row simulations).

Cases	$L_x \times L_y \times H$ (km ³)	S/D	$\langle C_P \rangle_{\text{row}}$	$\langle C_T \rangle_{\text{row}}$
Inf-H350-S2.5	$20 \times 9.6 \times 0.35$	2.5	0.6993	0.8894
Inf-H350-S5	$20 \times 9.6 \times 0.35$	5	0.6358	0.8347
Inf-H350-S10	$20 \times 9.6 \times 0.35$	10	0.6031	0.8058
Inf-H350-S20	$20 \times 9.6 \times 0.35$	20	0.5895	0.7936
Inf-H350-S40	$20 \times 9.6 \times 0.35$	40	0.5818	0.7866
Inf-H500-S2.5	$20 \times 9.6 \times 0.50$	2.5	0.6639	0.8588
Inf-H500-S5	$20 \times 9.6 \times 0.50$	5	0.6172	0.8181
Inf-H500-S10	$20 \times 9.6 \times 0.50$	10	0.5969	0.7998
Inf-H500-S20	$20 \times 9.6 \times 0.50$	20	0.5842	0.7887
Inf-H500-S40	$20 \times 9.6 \times 0.50$	40	0.5802	0.7849
Inf-H700-S2.5	$20 \times 9.6 \times 0.70$	2.5	0.6386	0.8366
Inf-H700-S5	$20 \times 9.6 \times 0.70$	5	0.6051	0.8069
Inf-H700-S40	$20 \times 9.6 \times 0.70$	40	0.5757	0.7809
Fin-H500-S2.5	$20 \times 50 \times 0.50$	2.5	0.6113	0.8128
Fin-H500-S5	$20 \times 50 \times 0.50$	5	0.6029	0.8054
Inf-H500-S5-stag	$20 \times 9.6 \times 0.50$	5	0.6169; 0.6156	0.8177; 0.8166
Inf-H500-S10-stag	$20 \times 9.6 \times 0.50$	10	0.5922; 0.5939	0.7965; 0.7982

mulation that does not define inlet and outlet areas of the control volume in advance (see Fig. 3).

Consider a control volume around a single turbine within a row or farm (Fig. 3) that is based on a streamtube, extending from the start of the induction zone until the end of the near wake. We choose the area $A_1 = SH$, which corresponds to the “available” inflow for the turbine. Note that the outlet area A_2 is a priori unknown but expected to be larger than A_1 . In the case of an infinite row of turbines, $A_2 = A_1$ is obtained. Moreover, similarly to Garrett and Cummins (2007) and Werle (2010), A_1 and A_2 do not need to be cylindrical, as the momentum theory is a one-dimensional analysis that does not intrinsically define the cross-sectional shapes. We refer to Fig. A1 in Appendix A for a visualization of the control volume around turbines in an infinite and a finite row,

based on the streamlines calculated from the LES. We further define the disc area $A_d = \pi D^2/4$ and the wake area A_w , which is not known a priori.

We presume uniform inflow U_{in} into the control volume and uniform pressures p_{in} and $p_{\text{in}} + \Delta p_{\text{NW}}$ over the inlet and outlet, respectively. Furthermore, the disc velocity $U_d = U_{\text{in}}(1 - a)$, with a being the axial induction factor. This leads to a thrust force $F_T = 1/2 \rho C_T U_{\text{in}}^2 (1 - a)^2 A_d$ and, in the absence of drag or mechanical losses, also to $P = 1/2 \rho C_T U_{\text{in}}^3 (1 - a)^3 A_d$.

First, applying the principle of conservation of mass on the streamtube that passes through the rotor and the entire

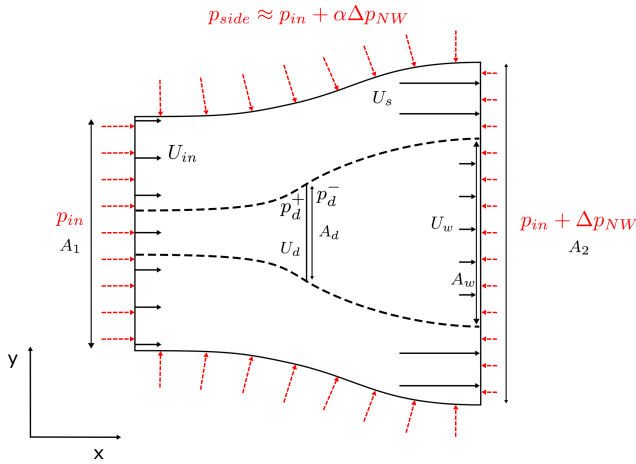


Figure 3. Top view of the general setup of the control volume around a turbine to define blockage effects.

streamtube, we obtain

$$A_d U_{in}(1-a) = A_w U_w, \quad (4)$$

$$A_w U_w + (A_2 - A_w) U_s = A_1 U_{in}. \quad (5)$$

Secondly, we apply the principle of conservation of momentum in the streamwise direction over the entire streamtube. Similar to Eq. (1), we presume that the friction at the ground is balanced by the background pressure difference present in the absence of a turbine ($F_{fric} \approx \Delta p_{bg}$); hence, to the first order, Δp_{NW} contains the pressure perturbations due to the presence of the wind turbines only. A similar strategy was used by, e.g., Kirby et al. (2023). As a result, the momentum balance equation is

$$\begin{aligned} -\frac{1}{2} C'_T U_{in}^2 (1-a)^2 A_d - \frac{1}{\rho} \alpha \Delta p_{NW} (A_1 + A_2) \\ = (A_2 - A_w) U_s^2 + A_w U_w^2 - A_1 U_{in}^2, \end{aligned} \quad (6)$$

where the density ρ is a known constant value. Here, we have further presumed that the average pressure on the mantle of the streamtube corresponds approximately to $p_{side} \approx p_{in} + \alpha \Delta p_{NW}$. Thirdly, using $F_T = (p^+ - p^-) A_d$, and eliminating p^+ and p^- using Bernoulli for streamlines in front of and behind the disc, respectively (similar to what is done in derivations of the classical Betz theory), we arrive at

$$\frac{1}{2} C'_T U_{in}^2 (1-a)^2 = \frac{1}{2} U_{in}^2 - \frac{1}{2} U_w^2 - \frac{1}{\rho} \Delta p_{NW}. \quad (7)$$

Finally, using Bernoulli for streamlines that do not pass through the rotor area, we also find

$$\frac{1}{2} U_{in}^2 = \frac{1}{\rho} \Delta p_{NW} + \frac{1}{2} U_s^2. \quad (8)$$

The above leads to a set of five model equations (Eqs. 4–8) with, in principle, four known input variables A_1 , A_d , C'_T , and

U_{in} , which leaves six unknown variables: a , U_w , U_s , A_w , A_2 , and Δp_{NW} . Thus, we lack one equation to arrive at a closed system.

There are two situations that lead to a simple closure of the system. First of all, imposing $\Delta p_{NW} = 0$ leads to the classical Betz–Joukowski theory for a single isolated turbine. The other case corresponds to an infinite row of turbines, in which case $A_2 = A_1 = SH$ (see Appendix A, Fig. A1a). This leads to the wind tunnel blockage corrections discussed earlier (e.g. Werle, 2010; Segalini and Inghels, 2014; note that a converging or diverging wind tunnel would require a known $A_2 \neq A_1$).

In the more general setting of a finite row of turbines, neither A_2 nor Δp_{NW} is known a priori. At the sides of a finite row, turbines clearly have more space to expand sideways, and possibly a lower Δp_{NW} applies than in the centre of the row, where the expansion of the inflow area A_1 is hindered by the surrounding turbines (see Appendix A, Fig. A1a). Thus, in such a system, a coupling through a larger pressure system can be expected, with a pressure gradient not only in the streamwise direction but also in the spanwise direction. An additional relation for the pressure system may be, e.g., obtained from an atmospheric perturbation model (Allaerts and Meyers, 2019; Devesse et al., 2022; Stipa et al., 2024; Devesse et al., 2024a, b; see also the open-source model WAYVE), which incidentally also parameterizes the more complex relation between capping inversion displacement and gravity wave excitation in wind farms. It is, however, not in the scope of the current work to develop such a coupling. Instead, we will evaluate the pressure system arising in our large-eddy simulations in more detail and use Δp_{NW} measured from the simulations as an additional input to evaluate the system above, comparing its output in terms of power and thrust with those obtained directly from LES.

4 Results and discussion

4.1 Velocity deficit and wake recovery

4.1.1 Induction zone and near-wake analysis

Here, we look in more detail into the wake development for the different simulation cases. In Fig. 4, we present the streamwise centreline velocity (U_c), scaled by the free-stream velocity at hub height (U_∞) and averaged over the turbines in each row, for all cases, providing a general overview of the differences and possible similarities in wake development. In Fig. 4a, two regions of interest are depicted, i.e. the induction zone and near wake on the one hand and the far wake on the other hand. We use the minimum of the velocity to mark the end of the near-wake region, which can depend significantly on the boundary layer height H as, e.g., seen in Fig. 4a. The start of the far-wake region is selected as $x/D = 6$ for all cases. As we will show below (see Fig. 6a and b), the far-wake velocity profile can be fitted very well

with a Gaussian function, which we can use to quantify the wake recovery behaviour in detail. Upstream of our selected starting point for the far wake, such a fit does not work very well, as the wake profile is transitioning from a top-hat to a Gaussian shape, potentially requiring more advanced fitting shapes.

First, looking at the near wake in Fig. 4, we observe that the maximum velocity deficit in the near wake decreases with S and H , i.e. with increasing blockage, for all cases. Consequently, we also expect the axial induction factor (a) to depend significantly on blockage. In Fig. 5, we show the axial induction factor for all cases, as obtained from the LES, as a function of the inverse geometrical blockage ratio ($A/A_d = 4SH/\pi D^2$), i.e. cases with strong blockage have a low inverse geometrical blockage ratio. We note that an alternative geometric blockage parameter based on the cross-section of the domain, i.e. $A_{\text{domain}}/A_{\text{farm}} = 4L_y H/N\pi D^2$, with L_y being the domain width, as, e.g., used for analysis of the tidal channels (see, e.g., Nishino and Willden, 2012), is not meaningful here, as, for our finite wind-farm simulations, we are considering $L_y \rightarrow \infty$. We evaluate $a = 1 - U_d/U_{\text{in}}$, with U_d being the disc averaged (and time averaged) velocity and U_{in} the turbine inflow velocity at hub height. For all infinite row cases, we also average over the different turbines in the row (as they have, in principle, the same induction factor); for the finite row cases, we show the induction of the individual turbines. For all cases, except the staggered row cases, U_{in} is simply the far upstream inflow velocity at hub height U_∞ , obtained from the concurrent precursor simulation. It is calculated as the streamwise velocity averaged along the streamwise line passing through the turbine hub location. For the staggered cases, particularly the second row, we observe, however, a significant acceleration of the flow upstream of the second-row turbines, which passes in between the turbines of the first row (see Fig. 4d). Therefore, for the second row, U_{in} is defined as the maximum velocity upstream of the turbine, which is located at the end of the near wake of the turbines in the first row (see Fig. 4d). Looking in particular at the comparison between the axial induction factor in the first and second row of the staggered row case and the single infinite row case, for the same boundary layer height (and thus the same inverse geometrical blockage ratio $A/A_d = 4SH/\pi D^2$), we observe that they are nearly equal and within averaging uncertainty, indicating that our choice of U_{in} works well. Later (see Sect. 4), we will show that this definition also leads to good performance of the simple model (Eqs. 4–8) when compared to LES data.

The error bars in Fig. 5 are constructed using moving block bootstrapping (MBB). Time averaging was performed over a time interval $T_{\text{av}} = 10\,000$ s, sampling every 2 s. The MBB method splits the original time series with n data samples into $N_b = n - L + 1$ overlapping blocks containing L samples. From this pool of N_b blocks, a new time series is assembled by randomly choosing $K = n/L$ blocks with replacement, and then the mean of the new time series is cal-

culated. This process is repeated B times, resulting in a distribution of means. Finally, the 2.5th and 97.5th percentiles of the distribution of means mark the 95 % confidence interval. The MBB approach is defined by selecting the number of bootstrapping runs B and the size of the blocks L . The preliminary sensitivity study showed convergence, for $L = 20$, to a robust value that does not significantly change for longer block lengths. A similar sensitivity study showed that $B = 1500$ iterations is sufficient for this purpose.

Looking further at Fig. 5a, we observe that the axial induction factor converges to $a \approx 0.264$ for a high inverse geometrical blockage ratio (A/A_d high). This is inline with the expected Betz–Joukowski value of $a = C'_T/(4 + C'_T) = 0.265$. The plot also shows that the finite row cases have an overall higher induction than their infinite row counterparts for the same inverse geometrical blockage ratio, implying that less blockage is present in the finite row cases. This will be explained further in Sect. 4.2.2. Overall, at low inverse geometrical blockage ratios (A/A_d low), we see a significant deviation of the induction factor towards values lower than the expected Betz–Joukowski value. This difference further translates towards the far wake, as seen before in Fig. 4. It is further interesting to look at the induced near-wake velocity. In Fig. 5b, we show $(1 - U_w/U_{\text{in}})/(2a)$, where U_w is evaluated as the minimum wake velocity (see Fig. 4) at hub height. Note that the expected Betz–Joukowski value of this ratio corresponds to 1. As can be seen in Fig. 5b, the induced near-wake velocity approaches the Betz–Joukowski value, for high inverse geometrical blockage, but some differences remain. In particular, the onset of wake recovery can reduce the maximum wake deficit expected from the pure inviscid solution predicted by Betz–Joukowski. Next to that, subtle effects related to the presence of shear may also play a role. When looking at decreasing inverse geometric blockage ratios, we observe that not only a lower induction occurs at the turbine disc but also an even lower wake deficit in the near wake (i.e. $(1 - U_w/U_{\text{in}}) < 2a$).

4.1.2 Far-wake analysis

We first discuss the evolution of the far wake as seen in a horizontal plane at hub height. Here, we observe that a classical Gaussian shape function provides good fits along the downstream direction. This is in line with Liu et al. (2002) and Shamsoddin and Porté-Agel (2017, 2018), who observed that the turbulent wake profiles retained a Gaussian shape under non-zero pressure gradient conditions. Thus, we use a Gaussian profile (Pope, 2000):

$$\frac{U_s(x) - u(x, y)}{U_s(x)} = C(x)e^{-y^2/(2\delta_y(x)^2)}, \quad (9)$$

where $U_s(x)$ is the streamwise velocity far from the wake centre, $u(x, y)$ is the wake velocity, $C(x)$ is the normalized wake velocity deficit, and $\delta_y(x)$ is the horizontal wake width. We fit this function to the LES data, thus extracting $U_s(x)$,

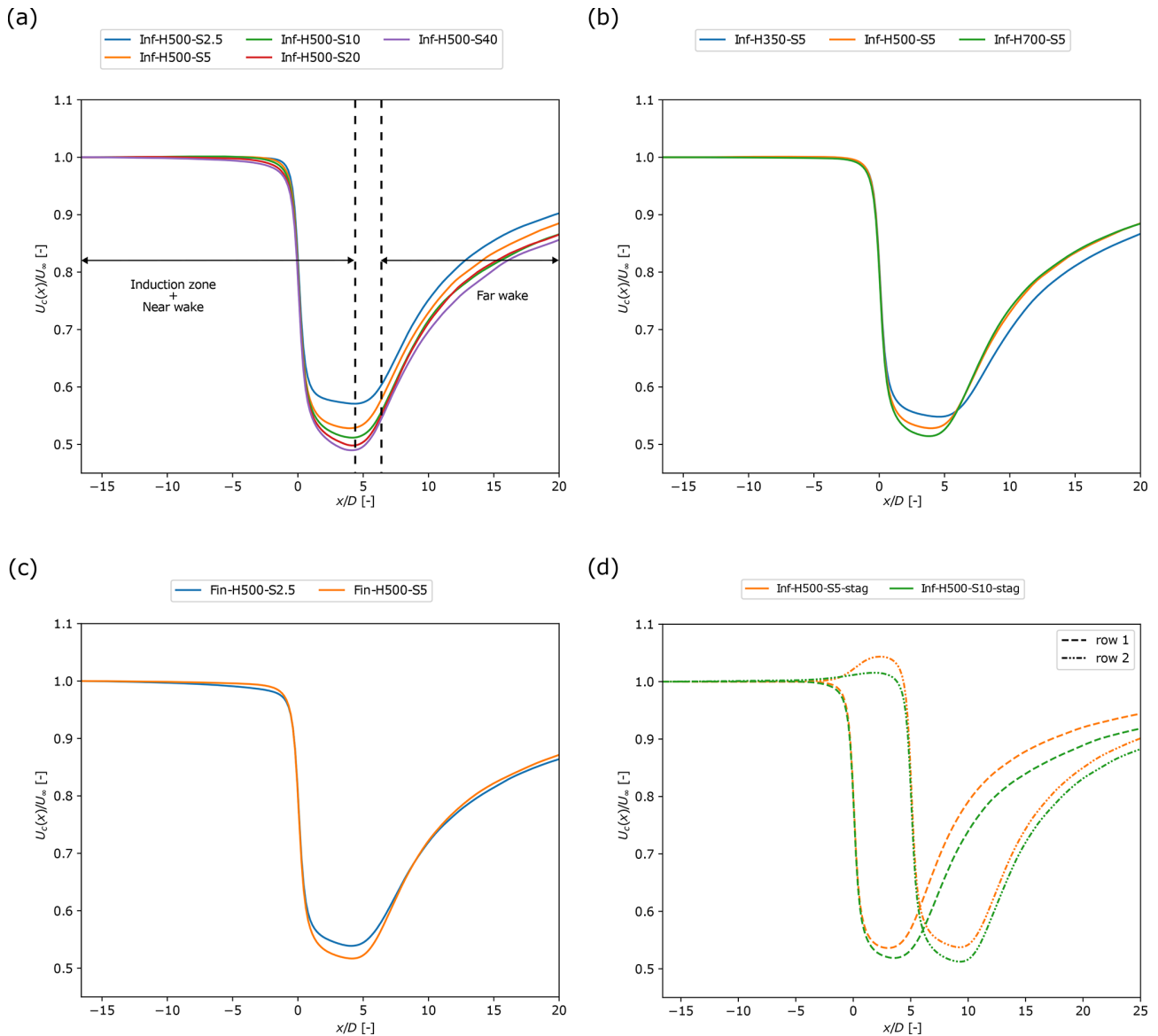


Figure 4. Streamwise centreline velocity U_c , scaled with the free-stream velocity U_∞ , averaged over all turbines within the row for (a) single infinite row cases with $H = 500$ m, (b) single infinite row cases with $S = 5D$, (c) finite row cases, and (d) staggered infinite row cases.

$C(x)$, and $\delta_y(x)$ as a result at each downstream position. Figure 6a and b show indeed that the horizontal wake profile, averaged across turbines in the row, has a Gaussian shape in the specified downstream range. Similar profiles are also found for all the other simulation cases.

Figure 7a–c show the evolution of $C(x)$, and Fig. 7d–f show the evolution of $\delta_y(x)$, averaged over the different turbines in each row, scaled with their values at the start of the far wake for all simulations. The downstream distance is reformulated as $(x - x_0)/\delta_{y,0}$, with x_0 being the starting location of the far wake. Figure 7b and e show that the far-wake development of the two infinite staggered rows, as well as the single finite row, follows the same trend as that of the single infinite row. As H increases, $C(x)$ shows a slightly steeper

decline, while $\delta_y(x)$ spreads faster. In particular, the difference between $H = 350$ m and the other two boundary layer heights is clearly visible. This can be understood by looking at the evolution of the vertical velocity profiles (in the wake centre) shown in Fig. 8 for infinite row cases with $S = 5D$. In particular for cases where $H = 350$ m, it is observed that vertical spreading of the wake is limited by the presence of the rigid lid, while the maximum wake deficit seems minimally impacted. Note that the turbine tip height (270 m) is not much lower than the boundary layer height in this case. Thus, for this case, the turbine far wake behaves less as an axisymmetric and more as a planar wake, which is known to have a lower spreading rate (Pope, 2000). We remark that the rigid lid reduces the overall wake spreading only at low

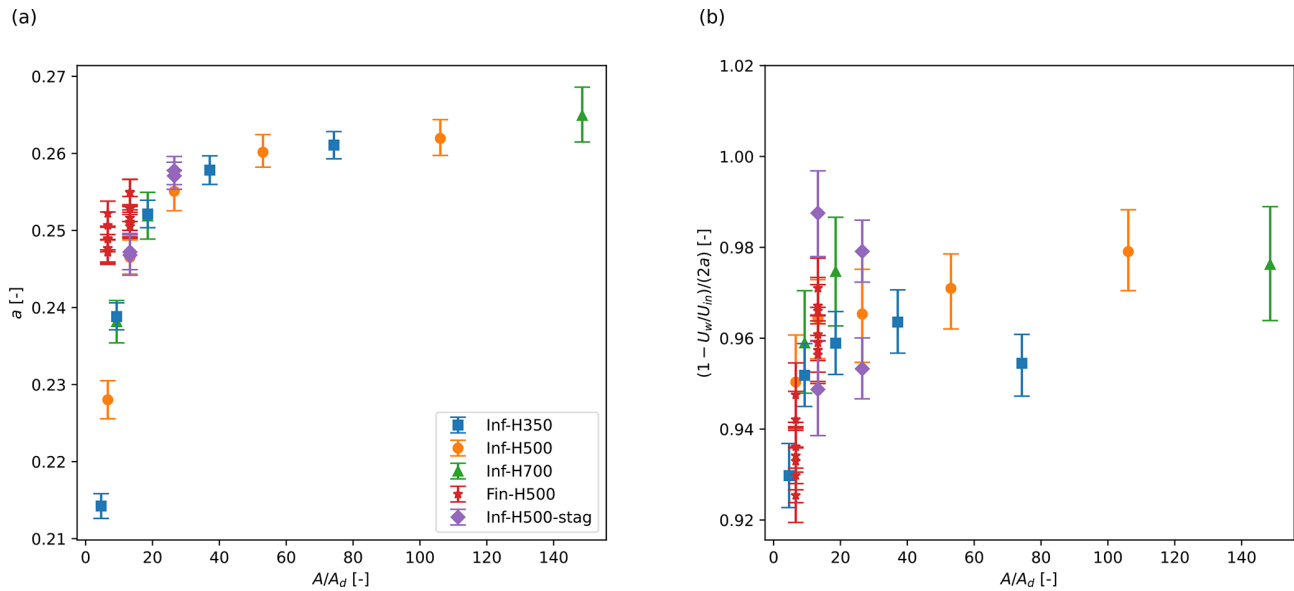


Figure 5. LES (a) axial induction factor a and (b) induced near-wake velocity scaled with the axial induction obtained, as a function of the inverse geometrical blockage ratio $A/A_d = 4SH/(\pi D^2)$. The row averages are shown for the infinite row cases, while individual turbine values are shown for the finite row cases. Error bars represent the 95 % confidence intervals, obtained using moving block bootstrapping.

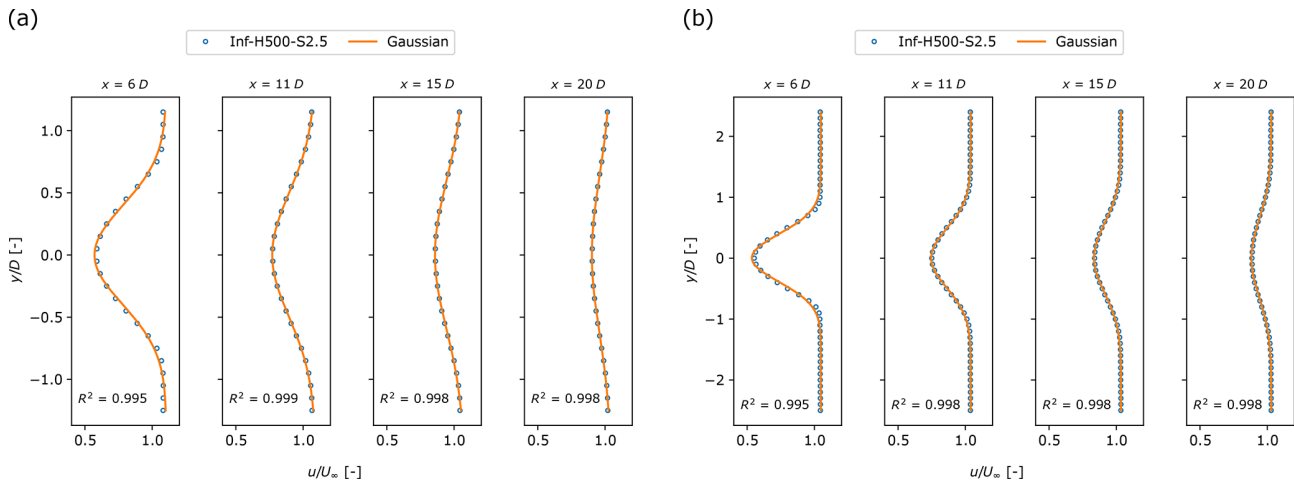


Figure 6. Horizontal wake velocity profiles, averaged over the turbines within the row, at different positions downstream in the far wake. The circles show LES results for the cases (a) Inf-H500-S2.5 and (b) Inf-H500-S5, and the orange lines represent the classical Gaussian shape function from Eq. (9). The R^2 value denotes the coefficient of determination.

H , while the wake recovery seems only slightly affected. We suggest that this imbalance is due to the unusual shape of the wake in the vertical direction for $H = 350$ m.

Returning to Fig. 7, we further observe that for constant H , the $C(x)$ and $\delta_y(x)$ curves align closely across varying S values and thus varying adverse pressure strengths. This contrasts with the findings of Liu et al. (2002) and Shamsoddin and Porté-Agel (2018), which suggest that a stronger adverse pressure gradient will slow down the wake deficit recovery and enhance wake spreading. However, the adverse pressure gradient in the far wake of our simulations (normal-

ized by ρU_{in}^2), turns out to be at least an order of magnitude smaller than the one in Liu et al. (2002) and Shamsoddin and Porté-Agel (2018), which they obtained as a result of diverging domain boundaries. Finally, looking back at Fig. 6a, which shows the turbine wake for the infinite row case Inf-H500-S2.5, which is periodic in the y direction, we see no uniform flow at the sides of the wake, starting from $x = 15D$. This implies that for cases with $S = 2.5D$ (and also $S = 5D$ for the two staggered rows), neighbouring wakes start touching around this downstream location. This also drastically changes the wake spreading rate, as wakes essentially start to

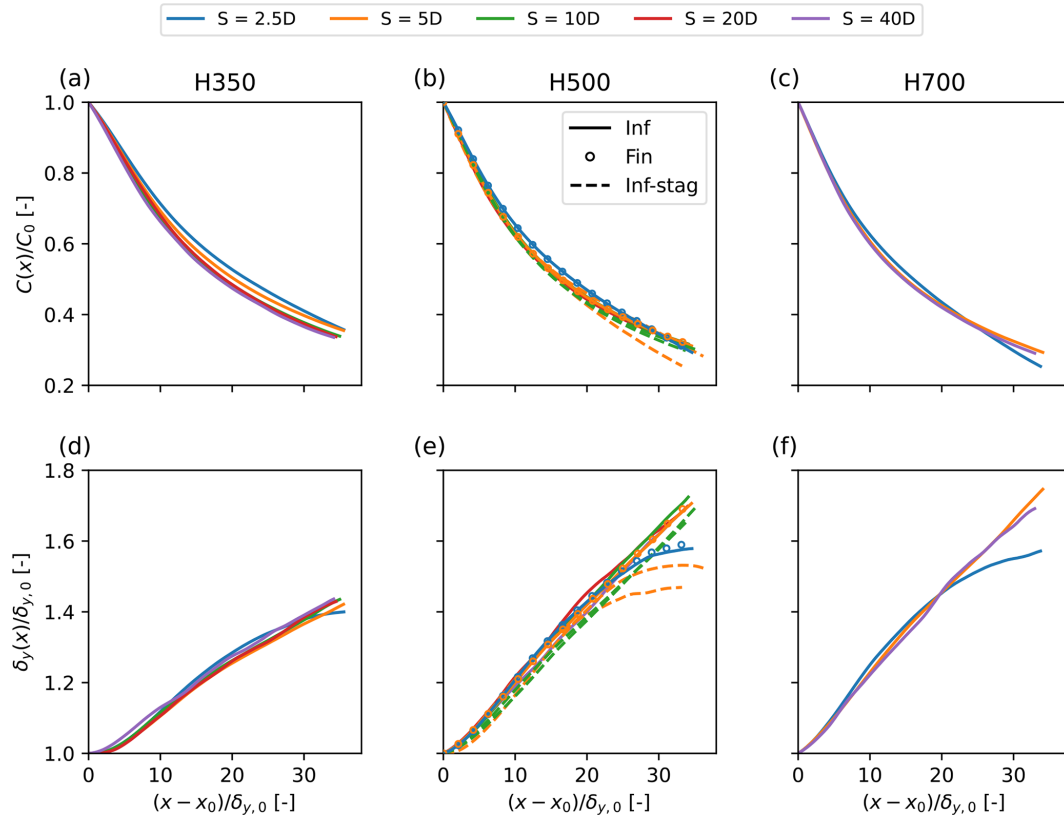


Figure 7. Evolution of the far-wake properties for all simulations, averaged over the turbines within the row. (a–c) Normalized wake velocity deficit $C(x)$ and (d–f) wake width $\delta(x)$, scaled with their respective value at the start of the far wake $C_0 = C(x_0)$ and $\delta_{y,0} = \delta_{y,0}(x_0)$, for various H , plotted against the downstream distance $(x - x_0)/\delta_{y,0}$, with $x_0 = 6D$ being the starting location of the far wake.

merge. We thus conclude that blockage has negligible direct effect on the far-wake recovery. Nevertheless, Fig. 4 shows a positive correlation between blockage and the near-wake deficit. Therefore, we suggest that blockage enhances wake efficiency, with the impact occurring primarily in the near wake.

4.2 Evaluation of the near-wake blockage model

We now focus on the effect of blockage on the power and thrust and evaluate the simple near-wake blockage model developed based on momentum theory (Eqs. 4–8) against the LES data. To this end, we evaluate from the large-eddy simulations:

$$C_P = \frac{F U_d}{\frac{1}{2} A_d U_{in}^3} = C'_T \left(\frac{U_d}{U_{in}} \right)^3 = C'_T (1 - a)^3, \quad (10)$$

$$C_T = \frac{F}{\frac{1}{2} A_d U_{in}^2} = C'_t \left(\frac{U_d}{U_{in}} \right)^2 = C'_t (1 - a)^2, \quad (11)$$

where a is evaluated as discussed above (see Sect. 4.1.1 and Fig. 5).

4.2.1 Infinite row

For the infinite row cases, all input variables ($A_1 = A_2 = SH$, A_d , C'_t , and U_{in}) required for the blockage model are known. U_{in} is obtained from the concurrent precursor as the streamwise velocity averaged over the streamwise line through the turbine hub location, except in the case of the second staggered row, where U_{in} is derived from the wind-farm simulation as the maximum velocity upstream of the turbine. We also briefly compare with calculating C_P and C_T in the LES using a rotor-disc-averaged velocity at rotor height in the precursor domain. In the results (not shown here), this produced similar C_P and C_T , with less than a 1 % difference for the highest blockage case. With C'_T fixed, C_P and C_T depend on the ratio U_d/U_{in} (i.e. the induction factor), which depends solely on the inverse geometrical blockage ratio. Thus, for varying U_{in} but constant SH , the model returns a single C_P and C_T value.

Figure 9a and c show $\langle C_P \rangle_{row}$ and $\langle C_T \rangle_{row}$ as a function of S/D , scaled with $C_{P,0}$ and $C_{T,0}$, which are the C_P and C_T values of a single freestanding turbine without blockage. To this end, we used the turbine in case Inf-H700-S40, as the geometric blockage ratio $A_d/A = 0.0067$, which can be regarded as negligible (Segalini and Inghels, 2014). As can

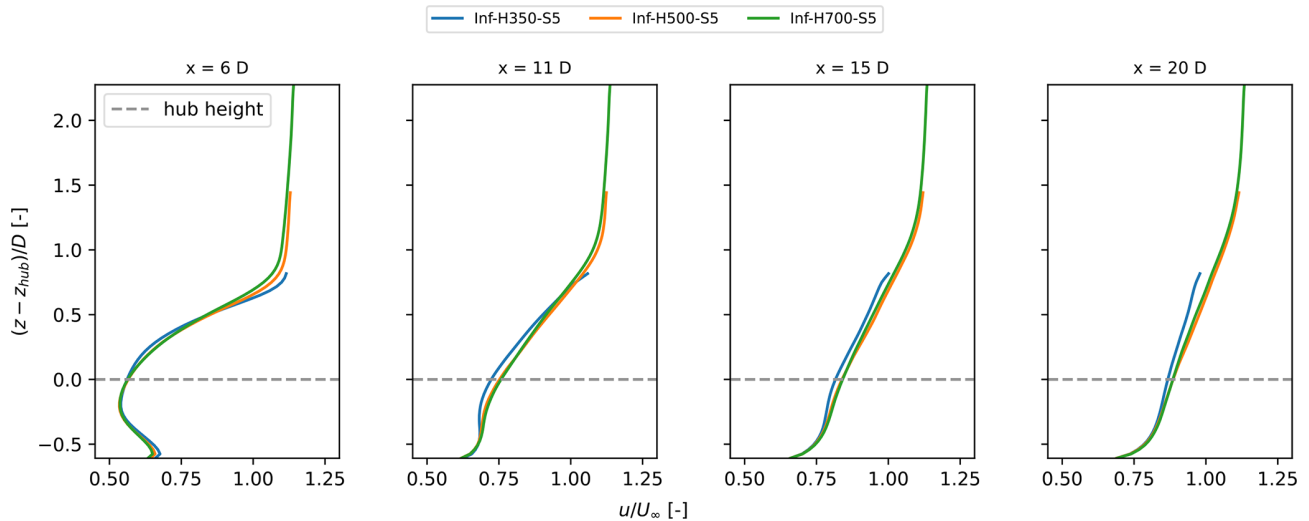


Figure 8. Vertical wake velocity profiles at different downstream positions, averaged over the turbines within the row for the infinite row turbine cases with $S = 5D$ and $H = 350, 500$, and 700 m.

be observed in the figure, the model agrees well with the LES data, although it tends to overpredict both thrust and power, particularly at high blockage ratios. We further see that at a turbine spacing of $S/D = 5$, there is a notable increase in $\langle C_P \rangle_{\text{row}}$ of 11 %, 8 %, and 5 % for $H = 350, 500$, and 700 m, respectively, compared to the single freestanding turbine.

Finally, Fig. 9b and d show $\langle C_P \rangle_{\text{row}}/C_{P,0}$ and $\langle C_T \rangle_{\text{row}}/C_{T,0}$ results from Fig. 9a and c as a function of the inverse geometrical blockage ratio (A/A_d). As mentioned above, the model output in this case depends only on the blockage ratio. We observe that the different LES results also collapse well onto a single curve when this scaling is used.

4.2.2 Finite row

For the finite row cases, the known input variables are $A_1 = SH$, A_d , C'_t , and U_{in} , which is obtained from the concurrent precursor as the streamwise velocity averaged over the streamwise line through the turbine hub location. For this case, the area A_2 is not known a priori, nor is the favourable pressure gradient known. This would require an additional closure relation that related the wind-farm thrust to the larger pressure system around the farm.

To appraise this large-scale pressure system, we evaluate for the finite row cases in Fig. 10a the pressure drop $-\Delta p_{\text{nw}}(y)$, containing only the pressure perturbations superimposed on the background pressure gradient (see Eq. 3). $-\Delta p_{\text{nw}}(y)$ is calculated as the difference between the domain inlet and the end of the near wake (defined as the location of maximum wake deficit), averaged over H , and shown as a function of the spanwise direction y , where $y = 0$ is located at the row centre. It is observed that the pressure drop reaches a maximum at the row centre, decreasing for

larger absolute values of y until a (near-zero) pressure difference is reached far from the turbine row. As expected, the wakes of turbines at the edge of the row have more space for lateral expansion and thus experience a lower $|\Delta p_{\text{NW}}|$ than those at the centre, where expansion is constrained by neighbouring turbines and the boundary layer height. This explains the overall lower axial induction found in the finite row cases compared to the equivalent infinite row cases, as seen in Fig. 5. All turbines in a finite row have fewer neighbouring turbines, resulting in a less constrained flow around the turbines. This can be considered as the collective blockage effect. Turbines within an infinite row are thus an extreme example of the centre turbines in a finite row. Additional simulations are needed to quantify the transition of a finite row into an infinite row, but this is beyond the scope of the current study. Looking in more detail at the pressure drop around the turbines, we see small local variations. These are partially related to the normal Reynolds stresses. For a conventional axisymmetric wake, it is well understood that $(1/\rho)\partial p/\partial r + \partial \overline{u'_r u'_r}/\partial r = 0$, with $\overline{u'_r u'_r}$ being the radial normal stress (Pope, 2000). Thus, in Fig. 10b, we have plotted $\Delta[p/\rho + \overline{v'v'}]$ as a function of y (and averaged over the boundary layer height). Note that the spanwise fluctuation v' is, strictly speaking, only in the radial direction in a horizontal plane, but as appreciated in the figure, the local variations in the pressure drop (in particular in the wake centres) disappear.

To close the system of Eqs. (4)–(8), we will use Δp_{NW} as observed in the LES and compare the thrust and power output of the near-wake blockage model with that of the LES. To obtain Δp_{NW} , we simply average $\Delta p_{\text{nw}}(y)$ over the interval $[y_h - S/2, y_h + S/2]$ for each turbine in the row. We note that a pressure closure at the farm level could, e.g., be provided by typical gravity wave models such as, e.g., WAYVE (Al-

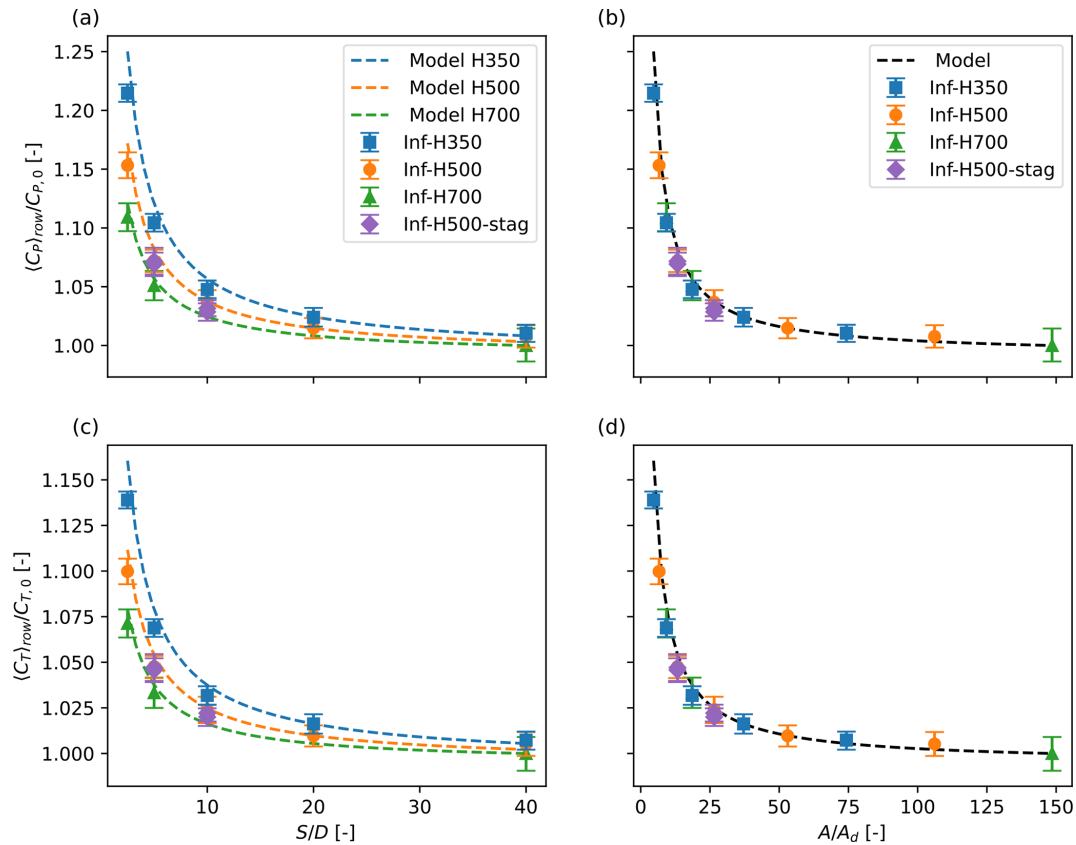


Figure 9. (a) Row averaged scaled power coefficient $\langle C_P \rangle_{\text{row}}/C_{P,0}$ as a function of spacing S/D and (b) as a function of inverse geometric blockage ratio A/A_d for varying boundary layer heights H . (c) Row averaged scaled thrust coefficient $\langle C_T \rangle_{\text{row}}/C_{T,0}$ as a function of S/D and (d) as a function of A/A_d for varying H . Data shown for all infinite row cases (single and staggered). $C_{P,0}$ and $C_{T,0}$ are the C_P and C_T of a single freestanding turbine with no blockage, i.e. case Inf-H700-S40. The error bars are bootstrap 95 % confidence intervals.

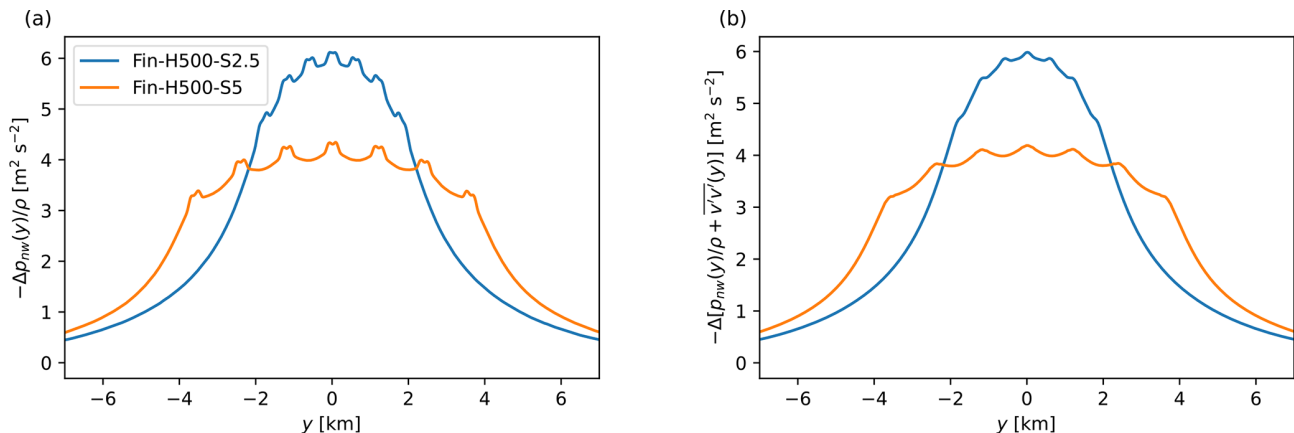


Figure 10. (a) Pressure drop at the end of the near wake ($-\Delta p_{\text{nw}}(y)$) and (b) pressure drop plus the lateral Reynolds stress ($\overline{v'v'}(y)$), averaged over H , as a function of the spanwise direction, where $y = 0$ km is the location of the centre turbine in the row.

laerts and Meyers, 2019; Devesse et al., 2022; Stipa et al., 2024; Devesse et al., 2024a, b), in which a coupling between the larger atmospheric flow around the farm and local wake models is foreseen. However, here, we aim specifically at assessing the relevance of a simple near-wake model that ac-

counts for a favourable pressure drop. A full interaction with the effects of gravity-wave feedback is a topic for future research.

In addition to closing the system with the pressure gradient from LES, we also evaluate the two-scale model pro-

posed by Nishino and Willden (2012, 2013) for half-open channel flows (formulated in the context of tidal turbines). At the turbine scale (i.e. the near-wake model), they use relations similar to Eqs. (4)–(8), while at the farm scale, they use classical Froude momentum theory without a pressure gradient to obtain a relation for the overall farm wake expansion. By further assuming that all turbines in a row produce the same power, they arrive at a closed system of equations. Although, the drawback of the approach is that there is no spanwise variation in turbine power output, it does allow for an overall assessment of farm power. We refer to Nishino and Willden (2012, 2013) for more details about this model and its implementation.

Figure 11a and b present the C_P and C_T for each turbine of cases Fin-H500-S2.5 and Fin-H500-S5, together with the predicted values from the extended Froude momentum theory model and the model developed by Nishino and Willden (2012). We notice that $\langle C_P \rangle_{\text{row}}$ is higher for the case with smaller S , i.e. stronger blockage, which was also observed for the infinite row cases. Additionally, the C_P value increases towards the row centre, with $C_{P,\text{centre}} > \langle C_P \rangle_{\text{row}} > C_{P,\text{side}}$, which was also found in the Reynolds-averaged Navier–Stokes results of Nishino and Draper (2015). The same findings are observed for the C_T data in Fig. 11b. We appreciate from the figures that, for the high blockage case (S2.5), both models overpredict the power. For the lower blockage case (S5), Nishino and Willden (2012, 2013)’s model is reasonably close to the row average predicted by the LES, whereas our model manages to predict also the shape of the power and thrust along the row rather well.

Finally, in Fig. 12, the power and thrust coefficients C_P and C_T are provided for all simulations, assembling the results from Figs. 9 and 11 into one figure. Overall, the model agrees well with the LES data, although it tends to overpredict both thrust and power, in particular at high blockage ratios, and for both the infinite and finite row cases, the error increases. We observe smaller increases in C_P and C_T for the finite row cases, compared to their infinite row counterparts, as less surrounding turbines are present to constrain the inflow from expanding, thus resulting in weaker pressure drops and blockage.

4.3 Discussion

To locate the origin of the model error, we perform a streamwise momentum budget analysis. The budget equation is derived by time-averaging the streamwise momentum equation and then integrating it over the control volume Ω , which is the same as the model’s control volume. In the streamwise direction, the control volume extends from the computational domain entrance to the end of the near wake (defined as the location with maximum wake deficit), $x_1 = 0$ to $x_2 = x_{\text{NW}}$. The vertical dimension of the control volume coincides with the vertical boundaries of the computational domain, that is, from $z_1 = 0$ to $z_2 = L_z$. Therefore, there is no

momentum flux across those faces. The lateral extension of the control volume follows the streamlines originating from the domain entrance at locations $y = y_{\text{hub}} \pm S/2$. Therefore, $(\bar{u}n_x + \bar{v}n_y) = 0$ and thus no advection of momentum across those faces (see Appendix A, Fig. A1, for a visualization of the streamlines). We denote x_1, x_2, s_1, s_2, z_1 , and z_2 as the boundaries of the control volume, where s represents the streamline coordinate. The y - z and x - y boundary faces are denoted by A_x and Ψ_z , respectively, while the s - z streamline boundary faces are denoted by Γ_s . By applying the divergence theorem to the streamwise momentum equation, the divergence operator is removed, allowing the conversion of the volume integral into a surface integral. The resulting equation is

$$\begin{aligned} & - \underbrace{\left[\int_{A_x} \bar{u} \bar{u} dA_x \right]_{x_1}^{x_2}}_{\Delta \mathcal{M}_{A_x}} - \underbrace{\left[\int_{A_x} (\bar{u}' u'^r + \tau_{xx}^{\text{sgs}}) dA_x \right]_{x_1}^{x_2}}_{\Delta F_{A_x}} \\ & + \underbrace{\sum_{j=1}^2 \left[\int_{\Gamma_s} ((\bar{u}' u'^r + \tau_{xx}^{\text{sgs}}) n_x + (\bar{u}' v'^r + \tau_{xy}^{\text{sgs}}) n_y) d\Gamma_s \right]_{/}}_{\Delta F_{\Gamma_s}} \quad (12) \\ & + \underbrace{\left[\int_{\Psi_z} \tau_{xz} n_z d\Psi_z \right]_{/}}_{\Delta \mathcal{F}_{\text{fric}}} - \int_{\Omega} \frac{1}{\rho_o} \frac{\partial \bar{p}_{\infty}}{\partial x} d\Omega \\ & - \underbrace{\int_{\Omega} \frac{1}{\rho_o} \frac{\partial \bar{p}^*}{\partial x} d\Omega}_{\mathcal{P}_x^*} + \underbrace{\int_{\Omega} \bar{f}_x d\Omega}_{\mathcal{F}_{t,x}} = 0 \end{aligned}$$

where $u' = u - \bar{u}$ and

$$\begin{aligned} \underbrace{\int_{\Omega} \frac{1}{\rho_o} \frac{\partial \bar{p}^*}{\partial x} d\Omega}_{\mathcal{P}_x^*} &= \underbrace{\left[\int_{A_x} \frac{1}{\rho_o} \bar{p}^* dA_x \right]_{x_1}^{x_2}}_{\mathcal{P}_{A_x}^*} \\ &+ \underbrace{\sum_{j=1}^2 \left[\int_{\Gamma_s} \frac{1}{\rho_o} \bar{p}^* n_x d\Gamma_s \right]_{/}}_{\mathcal{P}_{\Gamma_s}^*}. \quad (13) \end{aligned}$$

The term $\Delta \mathcal{M}_{A_x}$ describes the advection of streamwise momentum by the mean streamwise velocity, while ΔF_{A_x} accounts for the total (both resolved and modelled) turbulent transport of streamwise momentum along the streamwise direction. Further, $\Delta \mathcal{F}_{\text{fric}}^*$ captures the additional ground friction, not balanced by the background pressure gradient, due to the side flow acceleration induced by the turbines. Lastly, \mathcal{P}_x^* accounts for pressure gradients caused by wind-farm effects, and $\mathcal{F}_{t,x}$ stands for the turbine thrust force. By the sign

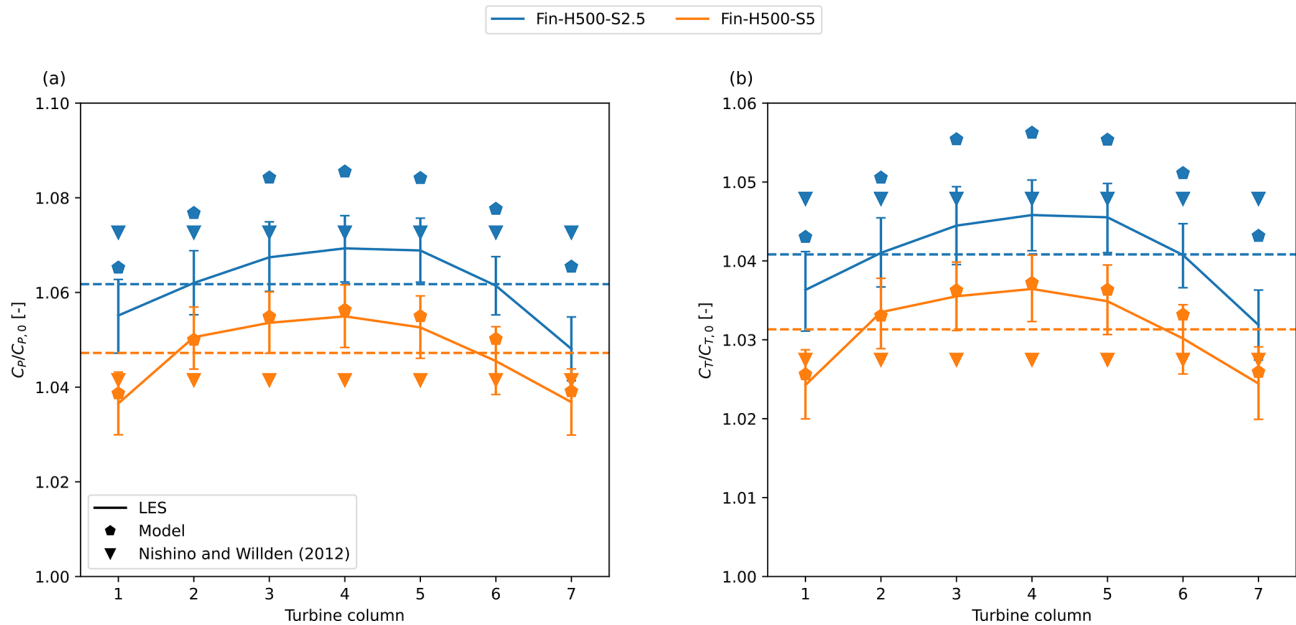


Figure 11. (a) C_p and (b) C_T for each turbine in the finite row cases, as found by the large-eddy simulations, the extended Froude momentum theory model, and the model from Nishino and Willden (2012). The error bars are bootstrap 95 % confidence intervals. Horizontal dashed lines mark the row averaged values of the corresponding LES cases.

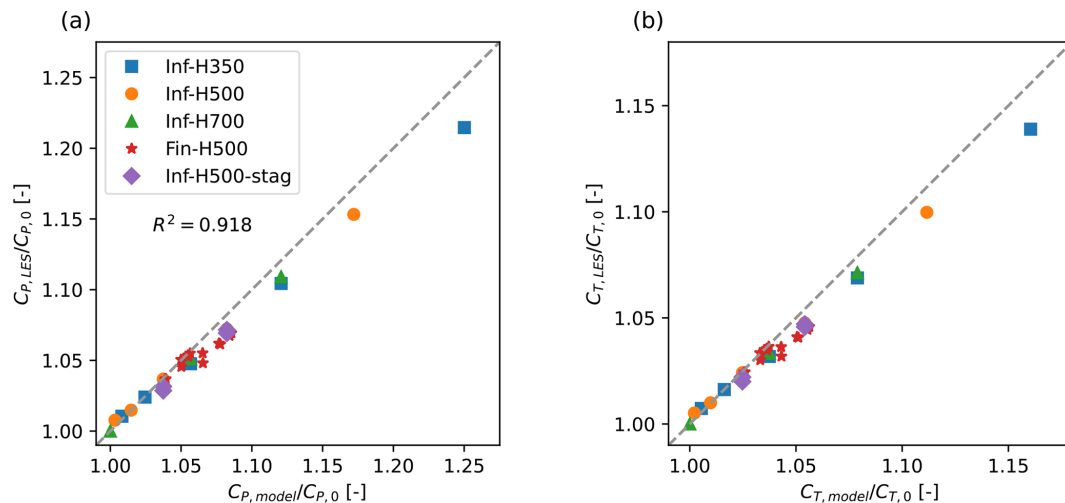


Figure 12. (a) The scaled power coefficient $C_{p,LES}/C_{p,0}$ and (b) the scaled thrust coefficient $C_{T,LES}/C_{T,0}$, as found by the extended Froude momentum theory model (x axis) and the large-eddy simulations (y axis). The squares, circles, and triangles represent the row averaged values of the single infinite row cases with respect to H . The stars represent the values of the individual turbines for the finite row cases. The diamonds represent the row averaged values of the infinite staggered row cases. The R^2 value denotes the coefficient of determination.

convention used, the first six terms in Eq. (12) are positive when the flow or turbulence brings more momentum into the control volume than out and negative when the opposite occurs. For instance, $\Delta \mathcal{M}_{A_x}$ is positive if the mean streamwise momentum integrated over A_{x_1} is greater than that over A_{x_2} . An increase in momentum along x would make this term negative.

The terms in the above equation are calculated and compared in Fig. 13 for the LESs and the model. We remark that, in the model, the terms $\Delta \mathcal{F}_{A_x}$, $\Delta \mathcal{F}_{T_s}$, and $\Delta \mathcal{F}_{fric}^*$ are not represented and therefore equal to 0. Figure 13a shows the comparison of the terms between the model and the LES for cases Inf-H350-S2.5 and Inf-H500-S2.5, scaled with the momentum flux going into the domain \mathcal{M}_{A_1} . It is clear that the model is capable of representing the dominant terms

($\Delta\mathcal{M}_{A_x}$, \mathcal{P}_x^* , and $\mathcal{F}_{t,x}$) in the momentum equation. More specifically, as also shown in Fig. 13b, the model can accurately predict the thrust yet overpredicts the magnitude of $\Delta\mathcal{M}_{A_x}$ and \mathcal{P}_x^* . This error increases for higher blockage cases. We identify three main causes for the overprediction of the model. First, the overprediction may partly be due to the model not accounting for the smaller remaining terms $\Delta\mathcal{F}_{A_x}$, $\Delta\mathcal{F}_{\Gamma_s}$, and $\Delta\mathcal{F}_{\text{fric}}^*$. For the infinite row cases, $\Delta\mathcal{F}_{\Gamma_s}$ is expected to be 0 because the control volume is not expanding (see Fig. A1a in Appendix A); therefore, the in- and outflowing turbulent momentum should be equal at the side boundaries. The term $\Delta\mathcal{F}_{A_x}$ could be added to the pressure term \mathcal{P}_x^* if $\overline{u'u'}$ has no direct effect on the thrust. Moreover, $\Delta\mathcal{F}_{\text{fric}}^*$ is stated to be 0 in the model, as we assumed that the ground friction is fully balanced by the background pressure gradient. The LES shows that the ground friction increases with the blockage strength and therefore $\Delta\mathcal{F}_{\text{fric}}^*$ is not 0, although the term is small. Secondly, the overprediction may be because of the poor representation of the near-wake velocity profile. The model assumes a top-hat function, whereas the LES already exhibits a smoothed top-hat profile. Therefore, the model will overpredict the streamwise momentum flux \mathcal{M}_{A_2} at the end of the near wake. Doubling the grid resolution of the LES in all three directions, as done for case Inf-H350-S2.5 in Fig. 13a and b, produces similar results. This suggests that within the current range of grid resolutions, the filter width of the actuator disc model has an insignificant effect on the near-wake shape. Thus, we conclude that the smoothed near-wake velocity profile is predominantly a result of turbulent mixing in the near wake. In future work, the model could be improved by defining the near-wake velocity profile with a shape function and parameterizing the near-wake energy as a function of the turbine thrust and ambient turbulence. Lastly, the overprediction could be due to the Shapiro correction. The correction was developed for a single turbine with no blockage. LES without the Shapiro correction shows that the correction introduces additional uncertainty for the highest blockage case (an $\approx 8\%$, 6% , and 4% increase for $\Delta\mathcal{M}_{A_x}$, $\Delta\mathcal{P}_x^*$, and $\Delta\mathcal{F}_{t,x}$ compared to the case without the Shapiro correction). In a future study, the turbines could be simulated using the actuator line model instead of the actuator disc model; this would circumvent the need for the correction.

Finally, we look at the finite row case Fin-H500-S2.5 in Fig. 13c and d. The conclusions drawn for the infinite row cases also hold for the finite row cases. We remark that now the model error on \mathcal{P}_x^* is drastically smaller because Δp_{NW} obtained from the LES is directly used as an input to the model. However, the error on this term is not zero because the model assumption of the side pressure $p_{\text{side}} = p_{\text{in}} + \alpha \Delta p_{\text{NW}}$, with $\alpha = 0.5$, is not entirely correct. The LES shows that p_{side} shifts closer to p_{in} , i.e. $\alpha < 0.5$; however, α depends on the blockage strength. Nevertheless, the contribution of p_{side} in the streamwise momentum balance is significantly smaller

than the other terms due to the small streamwise projection of the side surfaces.

5 Conclusions

This study set out to analyse the effect of blockage on the wake development behind turbines and the turbine power. Recent research by Lanzilao and Meyers (2024) discovered a strong positive correlation between the favourable pressure gradient in the farm and the wake efficiency η_w . This implies that the favourable pressure gradient, induced by blockage, enhances the wake recovery mechanism. We performed 17 LESs consisting of infinite and finite single turbine rows, as well as two staggered turbine rows, with constant C_T' , in an idealized atmospheric boundary layer setting. Blockage conditions were artificially introduced using a rigid lid, inducing a favourable pressure difference ($\Delta p_{\text{NW}} < 0$) over the turbine row and an adverse pressure difference ($\Delta p_{\text{FW}} > 0$) in the far wake. The blockage strength was adjusted by varying the turbine spacing ($S/D = 2.5, 5, 10, 20, 40$) and boundary layer height ($H = 350, 500, 700$ m).

A strong positive correlation was identified between Δp_{NW} and both the power coefficient (C_P) and thrust coefficient (C_T). Specifically, as S and H decrease, $-\Delta p_{\text{NW}}$, C_P , and C_T increase. Simultaneously, the rotor disc experiences lower induction, and the near wake shows a reduced wake deficit. Specifically, the infinite row cases, at realistic spacings $S/D = 5$, already show a significant increase in C_P of 11 %, 8 %, and 5 % for $H = 350, 500$, and 700 m, respectively, compared to a single freestanding turbine without blockage. Smaller increases are found for the finite row cases, as less surrounding turbines are present to constrain the inflow from expanding, thus resulting in weaker pressure drops and blockage. In this case, power and thrust are distributed and are maximum at the centre of the row, and $-\Delta p_{\text{NW}}$ increases towards the centre of the row.

The reduction in near-wake velocity deficit due to blockage also leads to smaller velocity deficits and narrower wake widths in the far wake. However, blockage has a negligible direct effect on far-wake development when scaling the far-wake deficit and width with their initial far-wake values. We note that the adverse pressure gradient in the far wake that we observed in our study is at least an order of magnitude smaller than those found by Liu et al. (2002) and Shamsoddin and Porté-Agel (2018) in diverging channels (for which case adverse effects on wake recovery were noticed). We thus conclude that the blockage enhances the wake efficiency, an effect that originates primarily from the lower near-wake deficit. However, we do see a profound effect of H on the wake spreading, with higher boundary layers leading to faster spreading. This relates to the fact that the wake can more freely expand vertically in high boundary layer cases into a larger region of high-speed flow than for shallow boundary layers.

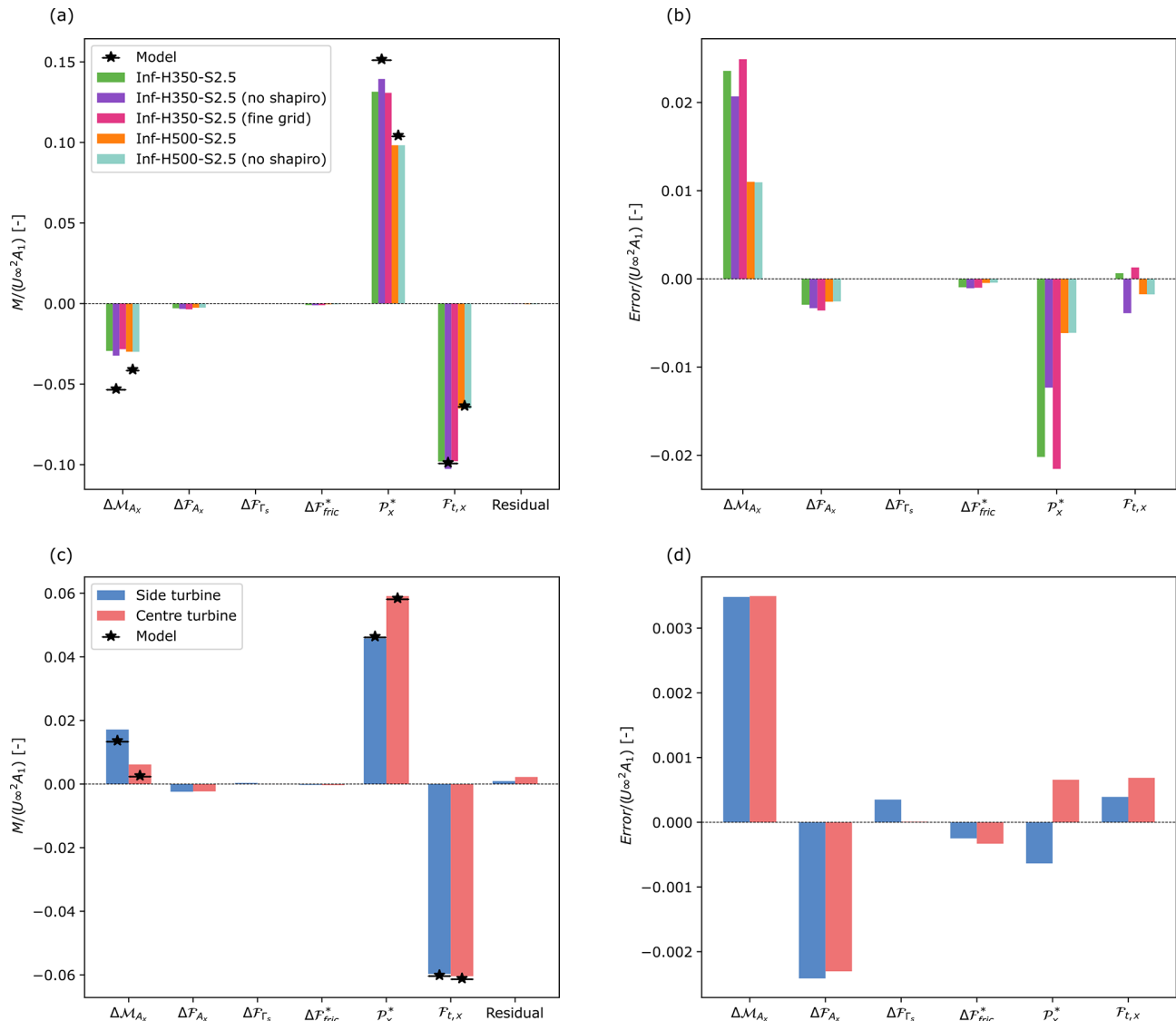


Figure 13. Comparison of the momentum sources and sinks as calculated by Eq. (12) between the developed model and the LES cases. (a) Row averaged results of the Inf-H350-S2.5 standard case, both with and without the Shapiro correction and with a finer grid, and of the Inf-H500-S2.5 standard case, both with and without the Shapiro correction. (c) Side and centre turbines of Fin-H500-S2.5. (b) and (d) show the corresponding model errors.

We further developed an analytical model consisting of five equations to predict the blockage effect on near-wake properties (similar to earlier models to correct for wind tunnel blockage in experiments – see Mikkelsen and Sørensen, 2002; Werle, 2010; Segalini and Inghels, 2014). Based on theoretical Froude momentum theory applied to a confined domain, the model uses five known input variables, i.e. rotor diameter (D), turbine spacing (S), boundary layer height (H), disc-based thrust coefficient (C'_T), and inflow velocity (U_{in}), but requires one additional closure relation. In the infinite row case, this is given by $A_1 = A_2$ (no expansion possible at the farm level), whereas in the finite row case, the near-wake pressure drop needs to be provided. To this end, we pro-

vided the pressure drop as measured in the large-eddy simulations. Overall, we found a good agreement between LES power and thrust predictions and the simple model based on momentum theory, indicating that the latter is a suitable candidate to improve turbine power prediction under blocking conditions. However, the model does underperform for the very high blockage cases. A momentum budget analysis identified the sources of the model overprediction, which can be improved primarily by parameterizing the near-wake velocity profile using a shape function, on the one hand, and possibly by parameterizing the ground friction, on the other hand. Furthermore, more detailed validation using LES in combination with an actuator line model, so that uncertain-

ties related to the Shapiro correction can be excluded, is also of interest. In a practical implementation, such a model needs to be coupled to a farm-scale model that provides input on the large pressure distribution in the farm. Atmospheric perturbation models (Allaerts and Meyers, 2019; Devesse et al., 2022; Stipa et al., 2024; Devesse et al., 2024b; see also the open-source model WAYVE) that explicitly model the pressure feedback coming from gravity waves are an interesting application for this. This is an ongoing topic of further research.

Appendix A: Control volume streamlines

This appendix aims to visualize the control volume around the turbines, as used in both the developed model and the momentum budget analysis. The control volume is bounded by streamlines derived from the time-averaged velocity fields of the LES, extending from the domain inlet to the end of the near-wake region. Figure A1a and b illustrate these streamlines at hub height for the infinite and finite row cases. For clarity, only four turbines are shown in each case. In the finite row case, these include the side turbine up to the row-centred turbine. We remark that the assumption $A_1 = A_2$ holds for the infinite row case, while $A_2 > A_1$ is valid for the finite row case.

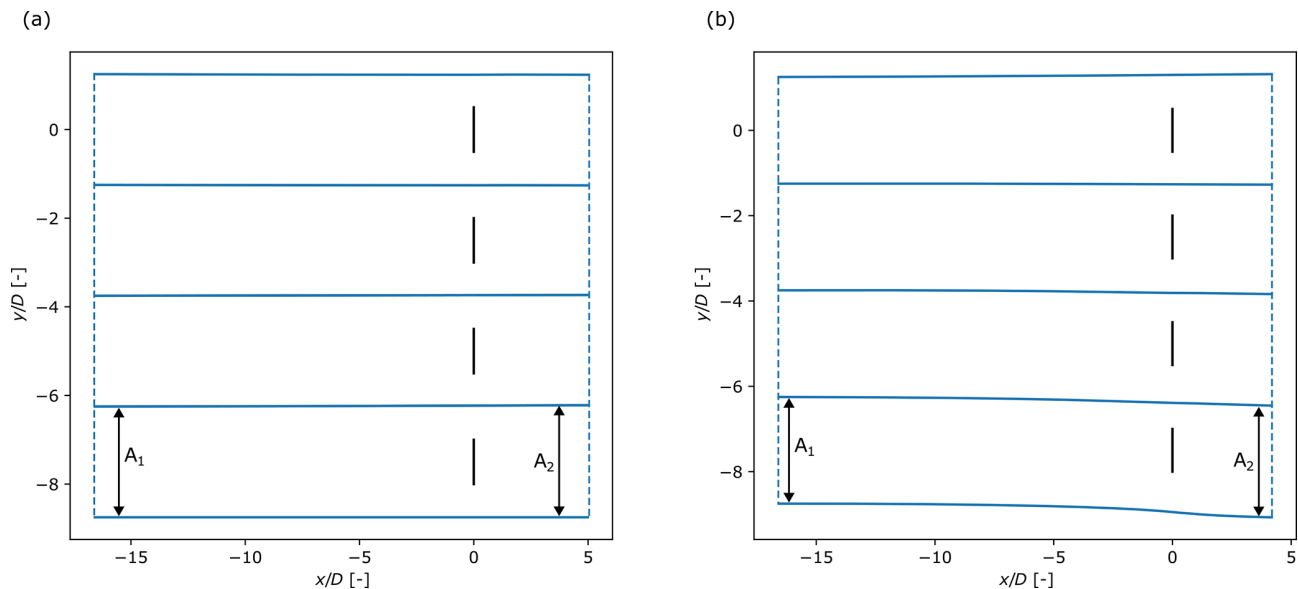


Figure A1. Plan view at hub height of four turbines in (a) case Inf-H500-S2.5 and (b) case Fin-H500-S2.5. The solid blue lines are the streamlines calculated from the LES. The blue dashed lines mark the beginning and end of the control volumes. The vertical black lines represent the turbines. The turbine at the centre of the finite row has coordinates $(x/D, y/D) = (0, 0)$, and at the edge, $(x/D, y/D) = (0, -7.5)$.

Code availability. The Navier–Stokes solver used in this work is SP-Wind, a proprietary software with restricted access. Access may be granted upon reasonable request.

Data availability. The full dataset generated during the study is available from the corresponding author upon reasonable request. The data and the Python scripts necessary to reproduce the figures in this study are openly available as a KU Leuven RDR dataset: <https://doi.org/10.48804/INE8OG> (Ndindayino, 2025).

Author contributions. ON and JM jointly defined the methodology and set up the simulation studies in the current work. ON, JM, and AP jointly developed the analytical models. ON carried out the simulations and post-processing. ON and JM wrote the paper.

Competing interests. At least one of the (co-)authors is a member of the editorial board of *Wind Energy Science*. The peer-review process was guided by an independent editor, and the authors also have no other competing interests to declare.

Disclaimer. Publisher's note: Copernicus Publications remains neutral with regard to jurisdictional claims made in the text, published maps, institutional affiliations, or any other geographical representation in this paper. While Copernicus Publications makes every effort to include appropriate place names, the final responsibility lies with the authors.

Acknowledgements. The computational resources and services used in this work were provided by the VSC (Flemish Supercomputer Center), funded by the Research Foundation – Flanders (FWO) and the Flemish Government. Additionally, the authors express their gratitude to the anonymous reviewers for their insightful comments and relevant observations on this work.

Financial support. This research has been supported by the Project Cloud4Wake, funded by Vlaamse Agentschap Innoveren & Ondernemen (VLAIO) under the Blue Cluster cSBO programme (contract no. HBC.2022.0549).

Review statement. This paper was edited by Cristina Archer and reviewed by three anonymous referees.

References

- Allaerts, D. and Meyers, J.: Boundary-layer development and gravity waves in conventionally neutral wind farms, *J. Fluid Mech.*, 814, 95–130, <https://doi.org/10.1017/jfm.2017.11>, 2017.
- Allaerts, D. and Meyers, J.: Gravity Waves and Wind-Farm Efficiency in Neutral and Stable Conditions, *Bound.-Lay. Meteorol.*, 166, 269–299, 2018.
- Allaerts, D. and Meyers, J.: Sensitivity and feedback of wind-farm-induced gravity waves, *J. Fluid Mech.*, 862, 990–1028, <https://doi.org/10.1017/jfm.2018.969>, 2019.
- Bleeg, J. and Montavon, C.: Blockage effects in a single row of wind turbines, *J. Phys. Conf. Ser.*, 2265, 022001, <https://doi.org/10.1088/1742-6596/2265/2/022001>, 2022.
- Bleeg, J., Purcell, M., Ruisi, R., and Traiger, E.: Wind Farm Blockage and the Consequences of Neglecting Its Impact on Energy Production, *Energies*, 11, 1609, <https://doi.org/10.3390/en11061609>, 2018.
- Calaf, M., Meneveau, C., and Meyers, J.: Large eddy simulation study of fully developed wind-turbine array boundary layers, *Phys. Fluids*, 22, 015110, <https://doi.org/10.1063/1.3291077>, 2010.
- Dar, A. S. and Porté-Agel, F.: Wind turbine wakes on escarpments: A wind-tunnel study, *Renewable Energy*, 181, 1258–1275, <https://doi.org/10.1016/j.renene.2021.09.102>, 2022.
- Devesse, K., Lanzilao, L., Jamaer, S., van Lipzig, N., and Meyers, J.: Including realistic upper atmospheres in a wind-farm gravity-wave model, *Wind Energ. Sci.*, 7, 1367–1382, <https://doi.org/10.5194/wes-7-1367-2022>, 2022.
- Devesse, K., Lanzilao, L., and Meyers, J.: A meso–micro atmospheric perturbation model for wind farm blockage, *J. Fluid Mech.*, 998, A63, <https://doi.org/10.1017/jfm.2024.868>, 2024a.
- Devesse, K., Stipa, S., Brinkerhoff, J., Allaerts, D., and Meyers, J.: Comparing methods for coupling wake models to an atmospheric perturbation model in WAYVE, *J. Phys. Conf. Ser.*, 2767, 092079, <https://doi.org/10.1088/1742-6596/2767/9/092079>, 2024b.
- Froude, R. E.: On the part played in propulsion by difference of fluid pressure, *Transactions of the Royal Institution of Naval Architects*, 30, 390–405, 1889.
- Gaertner, E., Rinker, J., Sethuraman, L., Zahle, F., Anderson, B., Barter, G. E., Abbas, N. J., Meng, F., Bortolotti, P., Skrzypinski, W., Scott, G. N., Feil, R., Bredmose, H., Dykes, K., Shields, M., Allen, C., and Viselli, A.: IEA Wind TCP Task 37: Definition of the IEA 15-Megawatt Offshore Reference Wind Turbine, technical Report, United States, March 2020, <https://doi.org/10.2172/1603478>, 2020.
- Garrett, C. and Cummins, P.: The efficiency of a turbine in a tidal channel, *J. Fluid Mech.*, 588, 243–251, <https://doi.org/10.1017/S0022112007007781>, 2007.
- Goit, J. and Meyers, J.: Optimal control of energy extraction in wind-farm boundary layers, *J. Fluid Mech.*, 768, 5–50, <https://doi.org/10.1017/jfm.2015.70>, 2015.
- Kirby, A., Dunstan, T. D., and Nishino, T.: An analytical model of momentum availability for predicting large wind farm power, *J. Fluid Mech.*, 976, A24, <https://doi.org/10.1017/jfm.2023.844>, 2023.
- Lanzilao, L. and Meyers, J.: Effects of self-induced gravity waves on finite wind-farm operations using a large-eddy simulation framework, *J. Phys. Conf. Ser.*, 2265, 022043, <https://doi.org/10.1088/1742-6596/2265/2/022043>, 2022.
- Lanzilao, L. and Meyers, J.: A parametric large-eddy simulation study of wind-farm blockage and gravity waves in conventionally neutral boundary layers, *J. Fluid Mech.*, 979, A54, <https://doi.org/10.1017/jfm.2023.1088>, 2024.
- Lignarolo, L. E., Mehta, D., Stevens, R. J., Yilmaz, A. E., van Kuik, G., Andersen, S. J., Meneveau, C., Ferreira, C. J., Ragni, D.,

- Meyers, J., van Bussel, G. J., and Holierhoek, J.: Validation of four LES and a vortex model against stereo-PIV measurements in the near wake of an actuator disc and a wind turbine, *Renewable Energy*, 94, 510–523, 2016.
- Liu, X., Thomas, F. O., and Nelson, R. C.: An experimental investigation of the planar turbulent wake in constant pressure gradient, *Phys. Fluids*, 14, 2817–2838, <https://doi.org/10.1063/1.1490349>, 2002.
- Maas, O.: Large-eddy simulation of a 15 GW wind farm: Flow effects, energy budgets and comparison with wake models, *Frontiers in Mechanical Engineering*, 9, <https://doi.org/10.3389/fmech.2023.1108180>, 2023.
- Martínez-Tossas, L. A., Churchfield, M. J., Yilmaz, A. E., Sarlak, H., Johnson, P. L., Sørensen, J. N., Meyers, J., and Meneveau, C.: Comparison of four large-eddy simulation research codes and effects of model coefficient and inflow turbulence in actuator-line-based wind turbine modeling, *J. Renew. Sustain. Ener.*, 10, 033301, <https://doi.org/10.1063/1.5004710>, 2018.
- Mason, P. J. and Thomson, D. J.: Stochastic backscatter in large-eddy simulations of boundary layers, *J. Fluid Mech.*, 242, 51–78, <https://doi.org/10.1017/S0022112092002271>, 1992.
- McTavish, S., Feszty, D., and Nitzsche, F.: A study of the performance benefits of closely-spaced lateral wind farm configurations, *Renewable Energy*, 59, 128–135, <https://doi.org/10.1016/j.renene.2013.03.032>, 2013.
- McTavish, S., Rodrigue, S., Feszty, D., and Nitzsche, F.: An investigation of in-field blockage effects in closely spaced lateral wind farm configurations, *Wind Energy*, 18, 1989–2011, <https://doi.org/10.1002/we.1806>, 2015.
- Meyers, J.: Error-Landscape Assessment of Large-Eddy Simulations: A Review of the Methodology, *J. Sci. Comput.*, 49, 65–77, 2011.
- Mikkelsen, R. and Sørensen, J.: Modelling of Wind Tunnel Blockage, in: 15th IEA Symposium on the Aerodynamics of Wind Turbines, FOI Swedish Defence Research Agency, 15th IEA Symposium on the Aerodynamics of Wind Turbines, Athens, Greece, 26–27 November 2001, 2002.
- Munters, W., Meneveau, C., and Meyers, J.: Turbulent Inflow Precursor Method with Time-Varying Direction for Large-Eddy Simulations and Applications to Wind Farms, *Bound.-Lay. Meteorol.*, 159, 305–328, <https://doi.org/10.1007/s10546-016-0127-z>, 2016a.
- Munters, W., Meneveau, C., and Meyers, J.: Shifted periodic boundary conditions for simulations of wall-bounded turbulent flows, *Phys. Fluids*, 28, 025112, <https://doi.org/10.1063/1.4941912>, 2016b.
- Ndindayino, O.: Replication Data for: Effect of blockage on wind turbine power and wake development, KU Leuven RDR, V1 [data set], <https://doi.org/10.48804/INE8OG>, 2025.
- Nishino, T. and Draper, S.: Local blockage effect for wind turbines, *J. Phys. Conf. Ser.*, 625, 012010, <https://doi.org/10.1088/1742-6596/625/1/012010>, 2015.
- Nishino, T. and Willden, R.: The efficiency of an array of tidal turbines partially blocking a wide channel, *J. Fluid Mech.*, 708, 596–606, <https://doi.org/10.1017/jfm.2012.349>, 2012.
- Nishino, T. and Willden, R.: Two-scale dynamics of flow past a partial cross-stream array of tidal turbines, *J. Fluid Mech.*, 730, 220–244, <https://doi.org/10.1017/jfm.2013.340>, 2013.
- Pope, S. B.: *Turbulent Flows*, Cambridge University Press, <https://doi.org/10.1017/CBO9780511840531>, 2000.
- Rankine, W. J. M.: On the mechanical principles of the action of propellers, *Transactions of the Institution of Naval Architects*, 6, 13, 1865.
- Sanchez Gomez, M., Lundquist, J. K., Mirocha, J. D., and Arthur, R. S.: Investigating the physical mechanisms that modify wind plant blockage in stable boundary layers, *Wind Energ. Sci.*, 8, 1049–1069, <https://doi.org/10.5194/wes-8-1049-2023>, 2023.
- Segalini, A. and Dahlberg, J.-A.: Blockage effects in wind farms, *Wind Energy*, 23, 120–128, <https://doi.org/10.1002/we.2413>, 2020.
- Segalini, A. and Inghels, P.: Confinement effects in wind-turbine and propeller measurements, *J. Fluid Mech.*, 756, 110–129, <https://doi.org/10.1017/jfm.2014.440>, 2014.
- Shamsoddin, S. and Porté-Agel, F.: Turbulent planar wakes under pressure gradient conditions, *J. Fluid Mech.*, 830, R4, <https://doi.org/10.1017/jfm.2017.649>, 2017.
- Shamsoddin, S. and Porté-Agel, F.: A model for the effect of pressure gradient on turbulent axisymmetric wakes, *J. Fluid Mech.*, 837, R3, <https://doi.org/10.1017/jfm.2017.864>, 2018.
- Shapiro, C. R., Gayme, D. F., and Meneveau, C.: Filtered actuator disks: Theory and application to wind turbine models in large eddy simulation, *Wind Energy*, 22, 1414–1420, <https://doi.org/10.1002/we.2376>, 2019.
- Smith, R. B.: The wind farm pressure field, *Wind Energ. Sci.*, 9, 253–261, <https://doi.org/10.5194/wes-9-253-2024>, 2024.
- Sood, I., Simon, E., Vitsas, A., Blockmans, B., Larsen, G. C., and Meyers, J.: Comparison of large eddy simulations against measurements from the Lillgrund offshore wind farm, *Wind Energ. Sci.*, 7, 2469–2489, <https://doi.org/10.5194/wes-7-2469-2022>, 2022.
- Stevens, R. J., Graham, J., and Meneveau, C.: A concurrent precursor inflow method for Large Eddy Simulations and applications to finite length wind farms, *Renewable Energy*, 68, 46–50, <https://doi.org/10.1016/j.renene.2014.01.024>, 2014.
- Stipa, S., Ajay, A., Allaerts, D., and Brinkerhoff, J.: The multi-scale coupled model: a new framework capturing wind farm-atmosphere interaction and global blockage effects, *Wind Energ. Sci.*, 9, 1123–1152, <https://doi.org/10.5194/wes-9-1123-2024>, 2024.
- Strickland, J. and Stevens, R.: Effect of thrust coefficient on the flow blockage effects in closely-spaced spanwise-infinite turbine arrays, *J. Phys. Conf. Ser.*, 1618, 062069, <https://doi.org/10.1088/1742-6596/1618/6/062069>, 2020.
- Strickland, J. M. and Stevens, R. J.: Investigating wind farm blockage in a neutral boundary layer using large-eddy simulations, *Eur. J. Mech.-B/Fluids*, 95, 303–314, <https://doi.org/10.1016/j.euromechflu.2022.05.004>, 2022.
- Taylor, P. K. and Yelland, M. J.: The Dependence of Sea Surface Roughness on the Height and Steepness of the Waves, *J. Phys. Oceanogr.*, 31, 572–590, [https://doi.org/10.1175/1520-0485\(2001\)031<0572:TDOSSR>2.0.CO;2](https://doi.org/10.1175/1520-0485(2001)031<0572:TDOSSR>2.0.CO;2), 2001.
- Verstappen, R. and Veldman, A.: Symmetry-preserving discretization of turbulent flow, *J. Comput. Phys.*, 187, 343–368, [https://doi.org/10.1016/S0021-9991\(03\)00126-8](https://doi.org/10.1016/S0021-9991(03)00126-8), 2003.
- Werle, M. J.: Wind Turbine Wall-Blockage Performance Corrections, *J. Propul. Power*, 26, 1317–1321, <https://doi.org/10.2514/1.44602>, 2010.

Wu, K. L. and Porté-Agel, F.: Flow Adjustment Inside and Around Large Finite-Size Wind Farms, *Energies*, 10, 2164, <https://doi.org/10.3390/en10122164>, 2017.